

INFLUENCE OF CATION CHOICE ON MAGNETIC BEHAVIOR OF III-N DILUTE  
MAGNETIC SEMICONDUCTORS

By

RACHEL MARIAN FRAZIER

A DISSERTATION PRESENTED TO THE GRADUATE SCHOOL  
OF THE UNIVERSITY OF FLORIDA IN PARTIAL FULFILLMENT  
OF THE REQUIREMENTS FOR THE DEGREE OF  
DOCTOR OF PHILOSOPHY

UNIVERSITY OF FLORIDA

2005

## ACKNOWLEDGMENTS

Many people helped support the research presented in this dissertation, too many to list individually. I appreciate all that each person contributed. In particular, I thank each member of my research group, especially those who taught me the basics, requirements for success in my research. I also thank each member of my committee for the inspiring thoughts and insightful conversations. I have met many and learned much during my graduate career at UF.

## TABLE OF CONTENTS

	<u>page</u>
ACKNOWLEDGMENTS .....	ii
LIST OF TABLES .....	v
LIST OF FIGURES .....	vi
 CHAPTER	
1 INTRODUCTION TO DILUTE MAGNETIC SEMICONDUCTORS.....	1
2 THEORETICAL AND EXPERIMENTAL BACKGROUND AND INVESTIGATIONS .....	4
Experimental Progress in DMS .....	4
Focus on III-As.....	5
Extension to III-Ns .....	5
Theoretical Background.....	7
Free Carrier Mediated Model of Ferromagnetism in DMS .....	7
Percolation Picture of Ferromagnetism in DMS .....	8
3 SURVEY OF POTENTIAL DILUTE MAGNETIC SEMICONDUCTORS WITH ION IMPLANTATION .....	10
Ion Implantation Method Description .....	10
Survey of Ion Implanted AlN .....	11
Experimental Characterization and Results of Ion Implantation.....	12
4 THIN FILM ALLUMINUM NITRIDE DILUTE MAGNETIC SEMICONDUCTOR GROWTH AND OPTIMIZATION OF MAGNETIC PROPERTIES .....	22
Growth by Molecular Beam Epitaxy .....	22
Growth of Thin Film AlMnN .....	24
Crystallinity and Phase Structure .....	25
Magnetic Properties.....	26
Magnetic Mechanism .....	27
Growth of Thin Film AlCrN.....	28
Crystallinity and Phase Structure .....	29

Role of V/III on Growth and Magnetic Properties .....	30
Effect of Dopant on Ferromagnetism .....	30
5   THERMAL STABILITY INVESTIGATION .....	42
6   ALN AND GAN BASED DILUTE MAGNETIC SEMICONDUCTOR APPLICATIONS .....	50
Spin Filter Applications of AlN DMS .....	50
Device Structure and Design .....	50
Device Testing and Results .....	52
7   INVESTIGATION OF GADOLINIUM AS A MAGNETIC DOPANT .....	64
Introduction of a New Magnetic Dopant .....	64
Growth of GaN:Gd .....	64
Magnetic Properties of GaN:Gd .....	65
Thermal Stability Investigation of GaN:Gd .....	67
8   CONCLUSION.....	82
AlN-based DMS Survey .....	82
Impurity Comparison.....	83
Thermal Instability.....	84
Device Applications.....	84
Summary and Future Work .....	85
APPENDIX	
SUPERCONDUCTING QUANTUM INTERFERENCE DEVICE	
MAGNETOMETRY .....	86
Sample Measurement Method .....	87
Background Subtraction .....	88
LIST OF REFERENCES .....	89
BIOGRAPHICAL SKETCH .....	92

## TABLE

<u>Table</u>	<u>page</u>
4.1. Table featuring the lattice constant and electrical properties of AlMnN and AlCrN films.....	32

## LIST OF FIGURES

<u>Figure</u>	<u>page</u>
3.1 Powder x-ray diffraction scan of AlN implanted with Mn. No additional phases are observed as compared to undoped AlN.....	15
3.2 Powder x-ray diffraction scan of AlN implanted with Cr. Additional phases as compared to the AlN are shown in the figure. ....	16
3.3 Powder x-ray diffraction scan of AlN implanted with Co. Additional phases as compared to the AlN are shown in the figure. ....	17
3.4 Magnetization versus applied field trace of Mn+-implanted AlN at a temperature of 100K.....	18
3.5 Magnetization versus applied field trace of Cr+-implanted AlN at a temperature of 300K.....	19
3.6 Magnetization versus applied field trace of Co+- implanted AlN at a temperature of 300K.....	20
3.7 Magnetization as a function of temperature for Co+-implanted AlN. A magnetic field of 500 Oe was applied during the measurement. ....	21
4.1 Estimated saturation magnetization and estimated remanent magnetization of AlMnN. The film was grown with Mn cell temperature of 650°C and under a nitrogen flow of 1.3 sccm.....	33
4.2 Magnetization versus applied magnetic field for AlMnN at temperatures of 10K and 300K. The film was grown with a Mn cell temperature of 650°C and under a nitrogen flow of 1.3 sccm.....	34
4.3 Magnetization vs. applied field of the undoped AlN showing paramagnetic behavior.....	35
4.4 Magnetization versus temperature for films of either undoped AlN, single phase AlMnN, or Mn <sub>4</sub> N. ....	36
4.5 Reflection high energy electron diffraction photo of AlCrN film grown at a Cr cell temperature of 992°C. The photo depicts a 2D/3D pattern with one by three reconstruction. ....	37

4.6	Atomic force microscopy image ( $1\mu\text{m}$ by $1\mu\text{m}$ ) of AlCrN with an rms roughness value of approximately 11 nm.....	38
4.7	Magnetization versus nitrogen flow for AlCrN films grown at a substrate temperature of $780^{\circ}\text{C}$ and with a Cr cell temperature of $987^{\circ}\text{C}$ .....	39
4.8	Magnetization vs. applied field for the optimal AlCrN and AlMnN films. ....	40
4.9	Magnetization vs. temperature in the temperature range from 10K-50K for AlMnN and AlCrN. A difference in curvature is seen for the two materials.....	41
5.1	Estimated saturation magnetization for AlCrN at each anneal temperature. ....	46
5.2	Magnetization versus applied field measurements comparing the as-grown AlCrN to the post-anneal AlCrN. Very little magnetization is left after an anneal of the AlCrN at $700^{\circ}\text{C}$ .....	47
5.3	Magnetization versus temperature taken under an applied field of 250 Oe comparing as grown AlCrN to post-anneal AlCrN. ....	48
5.4	Powder x-ray diffraction scans comparing as grown AlCrN to post-annealed AlCrN. No second phases are apparent after the $700^{\circ}\text{C}$ anneal.....	49
6.1	Schematic of the all semiconductor tunneling magneto-resistance stack. The reference stack contained undoped AlN in place of the AlMnN layer, and all thicknesses remained the same. The dark squares represent ohmic contacts made to the top GaN:Si layer and to the underlying MOCVD GaN buffer.....	55
6.3	Mask design used for fabrication of all semiconductor device. Alignment marks are found at each corner and in the middle of the mask. The larger dark bars represent the area of the mesa of the device. The open, or light areas, represent where ohmic contact was made to the device. ....	56
6.4	Scanning electron micrograph of all semiconductor device. Top view shows top and bottom Ti/Au ohmic contact, the top of the mesa and the etched valley showing the MOCVD GaN buffer. ....	57
6.5	Current-voltage measurement of all semiconductor tunneling magneto-resistance device with and without an applied magnetic field. Open circles represent the I-V measurement taken without an applied field. Dark squares represent I-V measurement taken after application of a 4000 Oe field. Note that tunneling increases after the field is applied. ....	58
6.6	Resistance vs. applied field measurement taken at 5K for the all semiconductor reference device.....	59
6.7	Resistance vs. applied field taken at 300K for the all semiconductor tunneling magneto-resistance device.....	60

6.8	Dark field ZSTEM image taken of the all semiconductor tunneling magneto-resistance device. The dark AlMnN layer shows roughness indicating poor growth quality at the interface.....	61
6.9	Selected area diffraction pattern tunneling electron micrograph taken of the all semiconductor tunneling magneto-resistance device. The AlMnN spin filter layer is indicated with an arrow. Strain can be seen within the AlMnN layer as indicated in the photo. ....	62
6.10	Scanning electron micrograph of a tunneling magneto-resistance device with FeNi as a spin injector. From the photo, the degradation of the FeNi is visible on the contact pad. This degradation represents nearly 90% of the devices. The FeNi degraded during photolithography, most likely due to the use of solvents during processing. ....	63
7.1	Reflection high energy electron diffraction pattern of GaN:Gd, $T_{Gd} = 1050^{\circ}\text{C}$ . The picture shows a 2D/3D pattern with 1x3 reconstruction.....	70
7.2	Atomic force microscopy image representing GaN:Gd with rms roughness of 1.541 nm.....	71
7.3	Magnetization vs. applied field loop taken at 50K for GaN:Gd, with $T_{Gd} = 950^{\circ}\text{C}$ . Hysteresis is observed at 50K, but not necessarily at 300K or 350K. ....	72
7.4	Magnetization vs. applied field taken at 50K for GaN:Gd corresponding to $T_{Gd} = 1000^{\circ}\text{C}$ - $1100^{\circ}\text{C}$ . ....	73
7.5	Estimated saturation magnetization vs. inverse of Gd cell temperature plot which shows the optimal $T_{Gd}$ . ....	74
7.6	Magnetization vs. applied field loops taken at 50K, 300K, and 350K for GaN:Gd with $T_{Gd} = 1050^{\circ}\text{C}$ . ....	75
7.7	Magnetization vs. temperature for GaN:Gd with $T_{Gd} = 1050^{\circ}\text{C}$ . Note that the magnetization is significantly decreased near room temperature. ....	76
7.8	Estimated saturation magnetization vs. anneal temperature for GaN:Gd with $T_{Gd} = 1050^{\circ}\text{C}$ . ....	77
7.9	Magnetization vs. applied field comparing the as grown GaN:Gd to that annealed at $600^{\circ}\text{C}$ .....	78
7.10	Magnetization vs. temperature of GaN:Gd after $700^{\circ}\text{C}$ anneal. ....	79
7.11	Magnetization vs. applied field at 50K and 350K for GaN:Gd annealed at $700^{\circ}\text{C}$ .....	80
7.12	Magnetization vs. applied field at 300K for GaN:Gd annealed at $700^{\circ}\text{C}$ .....	81



Abstract of Dissertation Presented to the Graduate School  
of the University of Florida in Partial Fulfillment of the  
Requirements for the Degree of Doctor of Philosophy

INFLUENCE OF CATION CHOICE ON MAGNETIC BEHAVIOR OF III-N DILUTE  
MAGNETIC SEMICONDUCTORS

By

Rachel Marian Frazier

August 2005

Chair: Cammy Abernathy

Major Department: Materials Science and Engineering

With the increasing interest in spintronics, many attempts have been made at incorporating spin-based functionality into existing semiconductor technology. One approach, utilizing dilute magnetic semiconductors (DMS) formed via introduction of transition metal ions into III-Nitride hosts, would allow for integration of spin based phenomena into current wide bandgap device technology.

To accomplish such device structures, it is necessary to achieve single phase transition metal doped GaN and AlN which exhibit room temperature magnetic behavior. Ion implantation is an effective survey method for introduction of various transition metals into AlN. In ion implanted AlN, the Co and Cr doped films showed hysteresis at 300K while the Mn doped material did not. However, it is not a technique which will allow for the development of advanced spin based devices. Such devices will require epitaxial methods of the sort currently used for synthesis of III-Nitride optoelectronics.

One such technique, Gas Source Molecular Beam Epitaxy (GSMBE), has been used to synthesize AlN films doped with Cr and Mn. Room temperature ferromagnetism has been observed for AlMnN and AlCrN grown by GSMBE. In both cases, the magnetic signal was found to depend on the flux of the dopant. The magnetization of the AlCrN was found to be an order of magnitude greater than in the AlMnN. The temperature dependent magnetic behavior of AlCrN was also superior to AlMnN; however, the AlCrN was not resistant to thermal degradation.

An all-semiconductor tunneling magnetoresistive device (TMR) was grown with GaMnN as a spin injector and AlMnN as a spin filter. The resistance of the device should change with applied magnetic field depending on the magnetization of the injector and filter. However, due to the impurity bands found in the AlMnN, the resistance was found to change very little with magnetic field.

To overcome such obstacles as found in the transition metal doped AlN, another dopant must be used. One viable dopant is Gd, which due to the low concentration incorporated in the semiconductor matrix should provide a single impurity level within the DMS instead of an impurity band. The incorporation of Gd into GaN and AlN may be the ultimate dopant for these III-N based DMS.

## CHAPTER 1

### INTRODUCTION TO DILUTE MAGNETIC SEMICONDUCTORS

The evolving field of spin transport electronics (spintronics) has drawn great interest within the past decade. The main goal of spintronics is the utilization of the electron spin in conjunction with that of electron charge.<sup>1-7</sup> The potential dual role of spin and charge in spintronics is interesting not only from a fundamental solid state physics standpoint, but also from a practical device implementation view. Many new device capabilities and functionalities may be added when the electron spin is manipulated.<sup>1</sup>

There are numerous driving forces behind the field of spintronics. Some of these include the advantages of spin over charge. Spin may be easily manipulated by an external magnetic field, which results in less work required to change spin as compared to charge<sup>3</sup>, and there is potential for long coherence time with spin whereas charge is easily destroyed by scattering effects such as collisions with defects or other charges.<sup>2</sup> The use of spin in electronics may lead to devices unattainable by systems based on charge alone. These devices are proposed to be much smaller than current electrical devices, use less electricity, and may be powerful enough to compute what charge-based devices cannot.<sup>2</sup> The aforementioned advantages take use of the two channel conduction associated with spin transport<sup>4</sup> which is based on Mott's spin channel model<sup>8</sup>. Another possible advantage is the integration of electronic, optoelectronic and magnetoelectronic functions on a single chip, which would result in more variety of performance than current microelectronics.<sup>2</sup>

Spintronics is currently utilized in existing technology. In fact, the 1995 prediction of a huge industry<sup>5</sup> became reality in 2001 in the form of a \$1 billion per year industry.<sup>2</sup> The technology utilizes magnetoresistance, or resistance which depends on the relative orientation of spins.<sup>6</sup> The giant magnetoresistance (GMR) sandwich structure makes up a read head and memory storage cell which IBM uses to sense changes in magnetic fields in current memory technologies.<sup>6</sup> The GMR sandwich structure is a stack of ferromagnetic and nonmagnetic metal layers in which the resistance relies on the alignment of the spins within the magnetic layers. When the magnetic layers are aligned, the resistance is low and conversely, if the layers are antiparallel, the resistance is high. GMR effects are also incorporated into sensors and switches which require low power.<sup>1</sup>

Other memory devices based on spin dependent tunneling are being investigated. Similar to GMR cells, these use an insulator in place of the nonmagnetic metal which amplifies the magnetoresistance. Such tunneling magnetoresistive (TMR) devices benefit from the increase in magnetoresistance, however they rely on high uniformity of amorphous oxide layers over a large area.<sup>1</sup>

Commercialized devices such as the GMR read head, rely on ferromagnetic metals for their functionality. Devices which require gain, such as light emitting diodes and transistors, cannot be made solely of metal, therefore, a major breakthrough in spintronics will require semiconductor-based devices.<sup>9</sup> Much work has been done on spin transport from a ferromagnetic metal into a semiconductor to try and reproduce the GMR effect in semiconductors.<sup>9-12</sup> Most of these attempts used a semiconductor sandwiched between two ferromagnetic metal contacts. In all metal devices, magnetoresistance is

measured to be greater than 100%;<sup>10</sup> however, semiconductor-based devices achieve only ~1%.<sup>12</sup> It has been suggested that the low value of magnetoresistance found in the semiconductor device arises from the inefficient spin transport across the metal/semiconductor interface<sup>13</sup> which results from a conductivity mismatch at the interface. To alleviate this mismatch, researchers have turned to dilute magnetic semiconductors.<sup>13-18</sup> Dilute magnetic semiconductors (DMS) differ from ordinary semiconductors in that they have local magnetic moments at the cation sites of the crystal structure.<sup>14</sup> The advantages of DMS include bandgap tunability, which allows for operation over a wide range in the electromagnetic spectrum, from far infrared to deep UV.<sup>15</sup> The use of DMSs would also allow for lattice matching. Furthermore, both of these advantages enable the possibility of spintronics incorporation into compound semiconductor technology,<sup>15</sup> something that is unattainable with the use of all metal devices.

## CHAPTER 2 THEORETICAL AND EXPERIMENTAL BACKGROUND AND INVESTIGATIONS

### Experimental Progress in DMS

The first materials studied for use as DMS include chalcogenides and the II-VI semiconductors. Both the II-VIs and the chalcogenides have very low Curie temperatures ( $T_C$ ), below 100K.<sup>19</sup> Device structures incorporating these materials prove the potential for spintronics, regardless of the low operating temperature (limited by the  $T_C$ ). One important example utilizes EuS as a spin filter by relying on tunneling magnetoresistance (TMR). During operation of this device, the magnetization of a layer of Gd and a layer of EuS is controlled by the application of an external magnetic field. The EuS acts as a tunnel barrier with the barrier height being dependent on the applied magnetic field through spin splitting of the conduction band at temperatures below the Curie point ( $T_C = 17K$ ). Tunneling is exponentially dependent on barrier height and therefore one spin channel has a higher probability of tunneling than the other. By reversing the magnetization within the EuS tunnel barrier, the tunneling current can be controlled, leading to TMR. Below  $T_C$ , the measured TMR is as large as 130%, indicating high spin efficiency. However, at 30K almost no TMR is observed, demonstrating the inability to incorporate EuS into current technology due to the extremely low operating temperatures.<sup>20-22</sup>

The first III-V semiconductor system studied for DMS material was the InAs system. It was found that a low growth temperature was necessary for the creation of a homogenous InMnAs alloy.<sup>20,21</sup> A higher growth temperature results in the segregation of

the Mn dopant, or clustering of the Mn.<sup>20,23</sup> N-type InMnAs is known to be paramagnetic<sup>20</sup>, and p-type InMnAs is ferromagnetic.<sup>21,22</sup> However, the Curie temperature of InMnAs is only 7.5K,<sup>21,22</sup> much too low for the incorporation of the material into devices.

### **Focus on III-As**

The focus turned to the GaAs<sup>24-28</sup> system due to the extensive use of GaAs in microwave and telecommunications technology.<sup>24</sup> The GaAs system is more promising than the InAs system because the Curie temperature is higher. A range of Curie temperatures have been found for p-type GaMnAs, from 50K to 110K.<sup>24-27</sup> The Mn concentration was varied within GaMnAs and it was found that the increase in Mn content did not result in the expected increase in magnetization.<sup>26</sup> It has been established that this is due to self-compensation of the Mn acceptors. The structure of the Mn in the GaMnAs lattice, from a homogeneous system to a semiconductor matrix with transition metal precipitates, affects carrier type as well as magnetic properties.<sup>26</sup> Most GaAs studies have been limited to Mn as the transition metal dopant. However, GaAs doped with Cr has also been studied.<sup>28</sup> Preliminary results indicate that GaCrAs is superparamagnetic.<sup>28</sup> The acceptor level of Cr is much deeper than that of Mn in GaAs (0.89 eV for Cr as compared to 0.11 eV for Mn), which results in low mobility and low Hall voltages in GaCrAs.<sup>28</sup>

### **Extension to III-Ns**

Despite the fact that GaMnAs is more promising than InMnAs, the Curie temperature is still too low for efficient device operation. Therefore, it is necessary to develop a DMS with a Curie temperature above room temperature. One way is to explore the potential of other semiconductor host systems.

The predicted Curie temperature for GaMnN is greater than room temperature.<sup>29</sup> This prompted interest in GaN based DMS along with the potential spintronic applications into current GaN technology such as high temperature, high power devices and visible light emitting devices.<sup>30</sup> In contrast to the GaAs system, the GaN and AlN systems are difficult to dope, so in order to create a DMS, the material must be fabricated far from equilibrium.<sup>31</sup> Given the high melting point ( $T_{MP}$ ) of GaN, even non-equilibrium growth results in a higher growth temperature than used for GaN.<sup>31</sup> Many Curie temperatures have been reported for GaMnN. These range from about 25K to greater than room temperature.<sup>32-35</sup> One group has reported a Curie temperature of 940K, although this temperature was extrapolated from lower temperature data, and was not physically measured.<sup>33-34</sup>

Although Mn is by far the most popular transition metal incorporated into GaN, another impurity has drawn considerable interest recently. Unlike GaCrAs, which was found to be superparamagnetic,<sup>28</sup> GaCrN is strongly ferromagnetic.<sup>37-38</sup> In fact, recent experimental investigation shows that GaCrN is ferromagnetic to above 900K.<sup>38</sup> In addition to Cr, there has been one report of strong ferromagnetism in GaN:Gd above room temperature,<sup>39</sup> which indicates yet another promising DMS.

Despite the experimental progress in bulk III-N DMS systems, there has been little experimental progress in device structures. There is evidence that quantum well structures of GaMnN separated by AlN enhance the magnetic signal as compared to bulk GaMnN.<sup>40</sup> However, other than first principle studies of spin injection at GaCrN/AlN interfaces,<sup>41</sup> there is no indication of the ability to incorporate the III-N DMS into spintronic devices.



In parallel to GaN, another system to note is that of AlN. Current applications of AlN include MIS heterostructures, gas sensors, heterojunction diodes and ultra-violet (UV) light emitting diodes (LEDs) and lasers. The fabrication of an AlN-based DMS has the potential of integrating spintronics into the previously mentioned technologies, the most important being UV applications. In fact, there is current interest in the Al-V DMS systems. Though AlMnAs was found to be paramagnetic<sup>42</sup>, the predicted Curie temperature of AlMnN is greater than room temperature.<sup>43</sup> AlCrN has been grown by reactive sputtering<sup>44</sup> and by molecular beam epitaxy.<sup>45</sup> In both cases, the Curie temperature was reported to be greater than room temperature.

### **Theoretical Background**

Although much research into DMS materials has been done,<sup>19-45</sup> there is not one single theoretical model which accurately fits the ferromagnetic behavior for all systems studied. Thus, it is necessary to review the main theoretical models and correlate them to the DMS systems which they apply.

### **Free Carrier Mediated Model of Ferromagnetism in DMS**

In the 1950s, Zener proposed a model of ferromagnetism appropriate for metals.<sup>46,47</sup> This model described ferromagnetism as driven by the exchange interaction between carriers and localized spins. However, it was later discovered that the Zener model left out critical criteria for the origin of ferromagnetism in metals.<sup>29</sup> The model did not take into account the itinerant character of magnetic electrons and it also neglected Friedel oscillations of electron spin polarization around localized spins. In an attempt to model ferromagnetism in DMS, Dietl<sup>48</sup> applied the Zener model to III-V and II-VI systems, arguing that the Friedel oscillations average to zero because in a DMS, the distance between the carriers is greater than the distance between the spins. This model is

the equivalent of the Ruderman-Kittel-Kasuya-Yosida (RKKY) interaction model. By taking into account the anisotropy of carrier-mediated exchange interaction associated with the spin-orbit coupling in the host material, the Curie temperature ( $T_C$ ) was found to be dependent on the hole concentration.<sup>29</sup> This is the basis for free-carrier mediated ferromagnetism. Much research has been done to try to prove that the RKKY interaction is most likely responsible for ferromagnetism in DMS.<sup>48-49</sup>

### **Percolation Picture of Ferromagnetism in DMS**

The free carrier mediated ferromagnetic model assumes very high carrier density, approximately  $10^{20} \text{ cm}^{-3}$ .<sup>49</sup> However, the model does not apply to low carrier systems. An alternative approach, which applies to both low and high carrier density GaAs systems, uses the percolation theory to calculate the ferromagnetic-to-paramagnetic transition temperature.<sup>50</sup> In order to explain this theory, a brief review of the polaron percolation model is necessary. Bound magnetic polarons (BMPs) form from the exchange interaction between localized carriers and magnetic impurities. BMPs consist of many magnetic impurities which interact with a localized carrier, say a hole. The direct exchange interaction between the impurities may be antiferromagnetic (for example, between Mn); however, the indirect exchange interaction between the BMPs can result in ferromagnetism.<sup>51</sup> The ferromagnetism arises due to the induced field between the magnetic impurities when the localized hole acts on these impurities. If the localized holes are parallel and the magnetic impurities are aligned with the holes, then the induced magnetic field is maximized and there is a ferromagnetic interaction.<sup>51</sup> When disorder of the hole positions is incorporated, there is a resulting enhancement of the ferromagnetic-to-paramagnetic transition temperature.<sup>50</sup> Numerical and analytical simulations suggest

that free carriers are not the only parameter affecting ferromagnetism in GaAs-based DMS.<sup>52</sup>

This percolation theory has also been applied to the III-Nitride system. The basis of the model relies on the difficulty of attaining a high concentration of free carriers in wide bandgap materials. In this situation, the RKKY interaction is not valid, and ferromagnetism arises from the indirect interaction between two magnetic ions.<sup>43</sup> Essentially, clusters of spins are formed and ultimately coalesce at what is known as the percolation threshold, which determines the ferromagnetic phase transition.<sup>43</sup>

## CHAPTER 3

### SURVEY OF POTENTIAL DILUTE MAGNETIC SEMICONDUCTORS WITH ION IMPLANTATION

#### **Ion Implantation Method Description**

Ion implantation is used in integrated circuit production lines to incorporate dopants into semiconductors with high uniformity and control. This is achieved by rastering a beam of ions at fixed energy across the semiconductor surface. Due to the surface bombardment at high energy, these ions are able to penetrate the semiconductor and incorporate into the host lattice. The projected range of the ions depends nearly linearly on the implantation energy. The dose of implanted dopant is determined by the flux of incident ions and is given by  $Q = Ft$  where  $Q$  is the dose,  $F$  is the flux of incident ions/cm<sup>2</sup>s and  $t$  is the implantation time.

During ion implantations, the semiconductor host lattice is damaged by the energetic ions. The host lattice atoms become displaced and crystal structure becomes disordered. For this reason, and to allow substitutional incorporation of the dopant ion, implanted semiconductors are thermally annealed at elevated temperatures. This generates sufficient energy to restore most of the crystal structure and allow dopant ions to move to substitutional sites within the host lattice. Although the post-implant anneal helps to recover lattice order, many implant-induced defects remain within the semiconductor lattice.

The advantages of ion implantation allow for applications in dilute magnetic semiconductors. Most prevalent is the use of ion implantation as a survey method in the

determination of choice of dopant and host semiconductor. Ion implantation provides useful insight into the prospect of specific choice of semiconductor lattice and dopant in terms of magnetic efficiency. It is a cost effective and quick method to incorporate a predetermined amount of dopant and examine the plausibility of a given DMS. Implanted samples may be easily characterized by magnetic techniques to verify ferromagnetic behavior of a DMS. For this reason, ion implantation into AlN is addressed.

### **Survey of Ion Implanted AlN**

Epitaxial layers of 1  $\mu\text{m}$  AlN were grown by metal organic chemical vapor deposition (MOCVD) on sapphire ( $\text{Al}_2\text{O}_3$ ) substrates. Three dopant ions ( $\text{Cr}^+$ ,  $\text{Co}^+$ , and  $\text{Mn}^+$ ) were implanted into the MOCVD AlN. The implantation energy was 250 keV which corresponds to a projected range of 150 nm for each dopant ion. The dosage was set to  $3 \times 10^{16}$  dopant ions per square cm ( $\text{dopants}/\text{cm}^2$ ) for each case, corresponding to peak concentrations of dopant ions of approximately 3 atomic percent (at %) in the AlN. During the implantation, the substrates were heated and held around  $300^\circ\text{C}$  to promote dynamic annealing. To further reduce lattice disorder and encourage dopant incorporation onto substitutional Al sites, post-implant annealing was performed at  $950^\circ\text{C}$  for two minutes in a Heatpulse 610T rapid thermal anneal (RTA) system under a nitrogen ambient.

The implanted AlN samples were characterized to determine the phase structure, magnetization and defect inclusion arising from the implantation for each dopant ion. The phase of each material was determined via powder x-ray diffraction (XRD), the magnetization via superconducting quantum interference device (SQUID) magnetometry, and the defect inclusion via photoluminescence (PL). The results of the material

characterization determine the effectiveness of AlN as a DMS, and give a rapid comparison of potential dopants. These results are discussed in the next section.

### **Experimental Characterization and Results of Ion Implantation**

Photoluminescence (PL) spectra were taken at a temperature of 10K of implanted AlN samples after thermal anneal. Comparing the undoped AlN to Cr+, Co+, and Mn+ doped AlN gives insight into the defects arising from implantation. The undoped AlN shows strong band-edge emission at 6.05 eV and two broad emission bands at 3.0 and 4.4 eV. The two emissions not corresponding to the band gap of the material are most likely related with deep level impurities within the band gap of the AlN. The implanted AlN all show an absence of band edge emission, which suggests that the point defect recombination centers created during the implantation are stable against the thermal anneal. Each of the implanted AlN shows a band at 5.889 eV which represents lattice disorder induced by the implantation, since it is independent of the Cr+, Co+, and Mn+ species introduced into the host lattice. Essentially, there is little difference between the Cr+, Co+, and Mn+ implanted AlN, and expected dissimilarities between the undoped and implanted AlN, which correspond to recombination centers and lattice disorder arising from the implantation.

Powder x-ray diffraction (XRD) scans (Figures 3.1-3.3) of the ion implanted AlN reflect the phase structure of the material, with single phase material being the optimal situation. The XRD scan for the undoped AlN provides a useful reference to eliminate any peaks observed in the implanted films as host lattice contributions. The Mn+ implanted AlN shows no additional peaks as compared to the undoped AlN (Figure 3.1). This suggests that this material is single phase. Both the Co+ and Cr+ implanted AlN show additional peaks compared to the reference scan. These peaks correspond to  $Al_xCr_y$

and  $\text{Al}_x\text{Co}_y$  phases for the  $\text{Cr}^+$  implanted and  $\text{Co}^+$  implanted  $\text{AlN}$ , respectively. It is important to note that neither  $\text{Al}_x\text{Cr}_y$  nor  $\text{Al}_x\text{Co}_y$  phases are ferromagnetic, which suggests that the additional second phases contributed no ferromagnetic signal to the magnetic study.

Superconducting quantum interference device (SQUID) magnetometry data show magnetic properties of films. Two important traces, the magnetization dependence on applied field ( $M$  vs.  $H$ ) and the magnetization dependence on temperature ( $M$  vs.  $T$ ), are most frequently used to demonstrate ferromagnetism (FM) and the temperature range across which FM exists, respectively. Hysteresis observed in  $M$  vs.  $H$  loops demonstrates material with FM properties. Persistent FM through all temperatures indicates the material's retention of FM, and implies that the Curie point ( $T_c$ ) has not been reached. In all cases of magnetic dopants, the implanted  $\text{AlN}$  show hysteresis. The  $\text{Mn}^+$  implanted  $\text{AlN}$   $M$  vs.  $H$  trace at 100K shows FM (Figure 3.4). The 10K  $M$  vs.  $H$  also shows clear hysteresis, however, no clear hysteresis was observed at 300K. This suggests that the FM is severely diminished or nonexistent at room temperature. However, both  $\text{Cr}^+$  and  $\text{Co}^+$  implanted  $\text{AlN}$  demonstrate FM at 300K (Figure 3.5). For each implanted ion, clear and well-defined hysteresis is observed in the  $M$  vs.  $H$ . Also, the  $M$  vs.  $T$  trace for  $\text{Cr}^+$  and  $\text{Co}^+$  (Figure 3.7) further suggests FM to room temperature by the persistence of magnetic signal to 300K. The contrasting magnetic behavior at 300K of the  $\text{Mn}^+$  implanted  $\text{AlN}$  and the  $\text{Cr}^+$  and  $\text{Co}^+$  implanted  $\text{AlN}$  suggests that  $\text{Mn}^+$  is the least optimal choice of dopant in terms of magnetization for an  $\text{AlN}$ -based DMS. The optimal dopant would exhibit FM at room temperature, thereby allowing for incorporation of the DMS into current technology.

Thus, the implantation of Cr<sup>+</sup>, Co<sup>+</sup>, and Mn<sup>+</sup> into AlN provides useful insight into the prospects of AlN-based DMS. Each of Cr<sup>+</sup>, Co<sup>+</sup> and Mn<sup>+</sup> implanted AlN demonstrates an absence of band-edge emission in PL spectra. Mn<sup>+</sup> implanted AlN shows single phase material, whereas Cr<sup>+</sup> and Co<sup>+</sup> implanted AlN show multiphase material. However, the Cr<sup>+</sup> and Co<sup>+</sup> implanted materials exhibit FM at room temperature, but the Mn<sup>+</sup> implanted AlN does not. It is not expected that the additional phases found in the Cr<sup>+</sup> and Co<sup>+</sup> implanted AlN give rise to the FM at 300K since the secondary phases are not FM. In general, the use of ion implantation to introduce magnetic dopants into AlN suggest that Cr<sup>+</sup> and Co<sup>+</sup> are more magnetically active than Mn<sup>+</sup>, however, Mn<sup>+</sup> is more readily incorporated to produce single phase material. Hence, further investigation is necessary to confirm the initial survey.



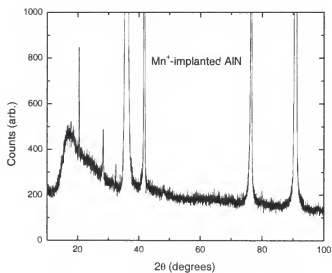


Figure 3.1. Powder x-ray diffraction scan of AlN implanted with Mn. No additional phases are observed as compared to undoped AlN.

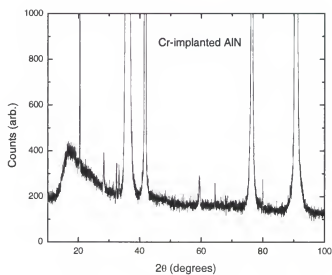


Figure 3.2. Powder x-ray diffraction scan of AlN implanted with Cr. Additional phases as compared to the AlN are shown in the figure.

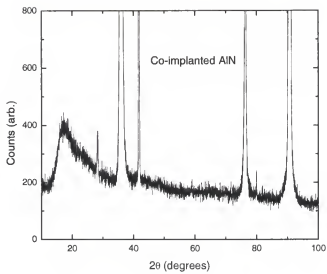


Figure 3.3. Powder x-ray diffraction scan of AlN implanted with Co. Additional phases as compared to the AlN are shown in the figure.

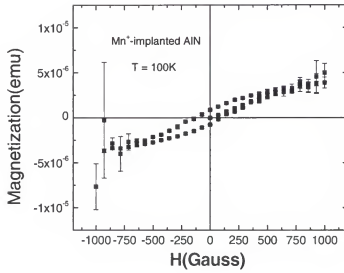


Figure 3.4. Magnetization versus applied field trace of Mn<sup>+</sup>-implanted AlN at a temperature of 100K.

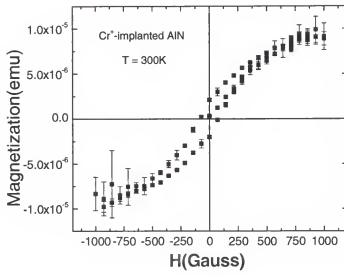


Figure 3.5. Magnetization versus applied field trace of Cr<sup>+</sup>-implanted AlN at a temperature of 300K.

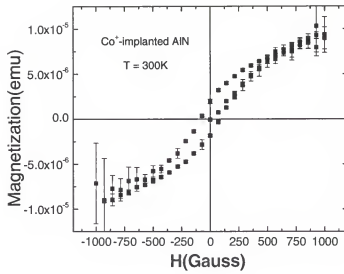


Figure 3.6. Magnetization versus applied field trace of Co<sup>+</sup>- implanted AlN at a temperature of 300K.

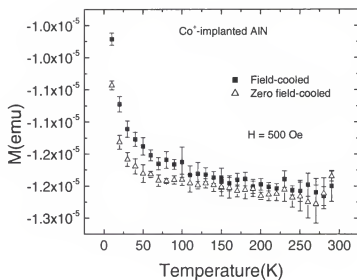


Figure 3.7. Magnetization as a function of temperature for Co<sup>+</sup>-implanted AlN. A magnetic field of 500 Oe was applied during the measurement.

CHAPTER 4  
THIN FILM ALLUMINUM NITRIDE DILUTE MAGNETIC SEMICONDUCTOR  
GROWTH AND OPTIMIZATION OF MAGNETIC PROPERTIES

**Growth by Molecular Beam Epitaxy**

In order to produce single crystal material with minimum defects, an epitaxial (epi) growth method is required. For this reason, the main growth method used in the fabrication of thin films is molecular beam epitaxy (MBE). During MBE growth, molecular beam constituents react with a heated crystalline substrate under ultra-high vacuum (UHV) conditions. The molecular beams are produced when solid, high purity metals are heated within a Knudsen cell (k-cell). In the growth of the epi III-Vs discussed in this paper, the group III and magnetic impurities were metal sources with 7N purity. The group V source was produced by inducing a plasma from a 7N purity nitrogen gas source, so the specific growth method is dubbed gas source molecular beam epitaxy (GSMBE). MBE, hence GSMBE, provides advantages over other epitaxy methods due to the ability to precisely control growth conditions such as substrate temperature, and group III and group V atoms impinging on the substrate surface. This allows for 1) a low growth rate, 2) the ability to abruptly initiate and/or terminate the growth, and 3) sharp interfaces and smooth surfaces, all of which provide the possibility of producing devices such as quantum wells, dots, and other structures relying on control of interlayers and interfaces. These MBE features also provide opportunity to monitor and characterize the growth surface in situ, including techniques such as reflection high energy electron diffraction, surface probe microscopy, and x-ray photoelectron spectroscopy.



The initial growth surface plays a role in the quality of the epitaxially grown overlayer. Hence, the choice of substrate impacts the MBE-grown film. For III-Ns (such as GaN, AlN, and AlGaIn) substrates include sapphire ( $\text{Al}_2\text{O}_3$ ), metal-organic chemical vapor deposition (MOCVD) GaN buffers on  $\text{Al}_2\text{O}_3$ , and silicon (Si) and silicon carbide (SiC). Each of these substrates has a different lattice match to the III-Ns. Impact of substrate choice on material properties such as magnetization will be presented later, however the preparation of each substrate prior to growth is slightly different. MOCVD GaN buffers are chemically treated prior to growth with a 1:1 HCl:DI  $\text{H}_2\text{O}$  3 minute dip, a 25 minute ultraviolet ozone ( $\text{UVO}_3$ ) exposure, and a 5 minute buffered oxide etch (BOE) dip. Each MOCVD GaN buffer is treated with this recipe prior to mounting to remove the native oxide on the GaN surface. Both Si and SiC receive a BOE dip to remove the native oxide, however the  $\text{Al}_2\text{O}_3$  substrate does not require a chemical treat prior to mounting. After any necessary chemical preparation, the substrates are mounted to Mo blocks with a thin In layer to provide thermal contact. The substrates are then loaded into the MBE system. The in situ treatment of the substrates differs due to the different lattice mismatch, and constituents of the substrate.  $\text{Al}_2\text{O}_3$  substrates require a nucleation layer of the III-N to initialize a decent growth surface, where as MOCVD GaN buffers do not, however both require an exposure to the N species prior to growth. Si and SiC substrates must not be exposed to N species prior to growth, or a silicide will form at the substrate surface and provide a poor growth surface.

During growth, the molecular beam species impinge on the substrate and undergo absorption and migration. Growth occurs when the impinging group III and group V atoms collide and stick to the surface, defined by the sticking coefficient which describes

how effectively the atoms stick to the surface. The three main growth conditions that affect the rate of growth are the flux of the group III species, the ratio of group V to group III flux of atoms (V/III) and the substrate temperature ( $T_s$ ). The effect of these growth conditions on the magnetic properties of the material under investigation are presented later in the chapter. Three distinct situations are possible during growth, which are affected by the growth conditions (V/III and  $T_s$ ). These growth modes are Frank-van der Merwe (layer by layer), Stranski-Krastanow (layer plus island) and Volmer-Weber (island). The growth mode of the film is monitored in situ by reflection high energy electron diffraction (RHEED), and represents the previously-mentioned growth modes by two dimensional (2D = line), combination of two dimensional and three dimensional (2D/3D = line and spots), and three dimensional (3D = spots) patterns, respectively.

The specific bulk epitaxial films grown and studied include AlN and GaN. The magnetic impurities introduced during growth include Mn, Cr, and Gd. The rest of the chapter serves to describe the different materials and the structural and magnetic properties arising due to the different growth conditions.

### **Growth of Thin Film AlMnN**

Growth of the films presented occurred in a Varian Gen II by gas-source molecular beam epitaxy. Solid Al(7N) and Mn(7N) sources were heated in standard effusion cells. Gaseous nitrogen was supplied by an Oxford rf plasma head. All films were grown on (0001) oriented sapphire substrates, indium mounted to Mo blocks. AlMnN and AlN films were grown at a temperature of 780°C, as indicated by the substrate heater thermocouple. A nitrogen flow of 1.3 standard cubic centimeters per minute (sccm) corresponded to a chamber pressure of  $2.3 \times 10^{-5}$  Torr during the growth of the films.

Sapphire substrates were first nitridated for 30 minutes at a substrate temperature of 1000°C under 1.1 sccm nitrogen (chamber pressure =  $1.9 \times 10^{-5}$  Torr). Nucleation at 575°C for 10 minutes and a 30 minute buffer layer at 950°C followed nitridation, both under 1.1 sccm nitrogen. Both AlN and AlMnN films were grown with a substrate temperature of 780°C and an Al effusion cell temperature of 1150°C. The Mn cell temperature ( $T_{Mn}$ ) was varied from 635°C to 658°C. The growth rate of the AlN was 0.2  $\mu\text{m/hr}$  and the growth rate of the AlMnN films was 0.16  $\mu\text{m/hr}$ .

In situ reflection high energy electron diffraction (RHEED) was used to monitor films during growth. AlN demonstrated 2D growth and AlMnN films demonstrated 2D/3D growth. Determination of the phase composition of the layers was carried out by x-ray diffraction in a Phillips APD powder diffractometer. AlMnN grown with a Mn cell temperature of 635°C was found to be single phase. The AlMnN with  $T_{Mn}=658^\circ\text{C}$  formed AlMn as detected by powder x-ray diffraction (XRD). A Mn cell temperature of 650°C was found to be the upper limit of single phase AlMnN under previously mentioned growth conditions. For comparison, a layer of  $\text{Mn}_3\text{N}_2$  was also grown on sapphire. Auger Electron Spectroscopy (AES) showed Mn to be present in all of the Mn films, however accurate determination of the Mn concentration in AlMnN was hindered by the small Mn signals. It is estimated that AlMnN films contain no more than 1% Mn.

### **Crystallinity and Phase Structure**

Crystalline quality of the films was inspected using high resolution x-ray diffraction (HRXRD) in a Philips X'pert diffractometer equipped with a  $\text{Cu K}\alpha$  source. Rocking curves were performed on films in order to determine the FWHM and lattice constants of the films. Lattice constants were calculated using Bragg's law from data

obtained by the HRXRD investigation. Table 1 shows results of those calculations for AlN and AlMnN grown using two different Mn cell temperatures. The lattice constant was found to decrease as the Mn cell temperature increased for single phase material. A similar pattern was observed for single phase GaMnN films grown in the same system under different conditions. GaN implanted with Mn has been reported to exhibit substitutional or near substitutional incorporation. It is expected that the incorporation of interstitial Mn should either increase or have no effect on the lattice constant. The observation of a decrease in the lattice constant of the AlMnN films suggests that the Mn occupies a substitutional site. This is further confirmed by Hall analysis, also given in Table I, which shows pure AlN to be highly resistive as expected and material containing an AlMn second phase to be highly conductive n-type. By contrast, single phase AlMnN was found to be p-type. If Mn incorporates substitutionally, one would expect by analogy with its behavior in other III-V materials that it would behave as a deep acceptor. The observation of p-type behavior fits this explanation.

### **Magnetic Properties**

Magnetic measurements were performed on samples using a Quantum Design MPMS SQUID magnetometer. Magnetization as a function of magnetic field and temperature was measured with the applied field parallel to all films. Magnetic remanence and coercivity indicating hysteresis was observed in ternary AlMnN films at 10, 100, and 300K. As a rough estimate, saturation magnetization was extracted from the hysteresis loops as the magnetization at 1000 Gauss (G). This estimated saturation magnetization was found to decrease at 300K compared to 100K for AlMnN grown at  $T_{\text{Mn}}=650^{\circ}\text{C}$ . Also, the remanent magnetization was extracted from the hysteresis loops

and was found to decrease with temperature. The values of temperature dependent estimated saturation magnetization and remanent magnetization of AlMnN are shown in Figure 4.1. A comparison of the M vs. H loops at 10K and 300K of the AlMnN shows a large decrease in observed hysteresis, as shown in Figure 4.2. This decrease in the overall magnetization as seen in the M vs. H loops possibly indicates that the Curie temperature of the AlMnN is just beyond 300K. However, clear hysteresis is evident at room temperature. The coercive field (approximately 70 Gauss) was found to be independent of temperature. Undoped AlN grown under the same conditions as AlMnN demonstrated paramagnetic behavior, as shown in Figure 4.3. This indicates that hysteresis arises with the addition of Mn. The diamagnetic background due to the sapphire substrate was subtracted from the raw data and the subsequent corrected data was used for analysis. The magnetization was not normalized to the Mn concentration due to the inability of AES to precisely detect the small amount of Mn in the films.

### **Magnetic Mechanism**

Clusters of second phases, undetectable by methods mentioned above, are not thought to be the cause of hysteresis observed at 300K. This is supported by magnetic analysis of material containing the most likely cluster phases, AlMn and Mn<sub>4</sub>N. Magnetization as a function of temperature for AlN, single phase AlMnN, AlMnN with an AlMn phase present, and Mn<sub>4</sub>N show substantially different behavior, as shown in Fig.4.4. The reason for the low T(10-50K) behavior seen in AlN and AlMnN films is still unknown. The M vs. T of Mn<sub>4</sub>N clearly indicates ferromagnetic behavior, and the formation of clusters has been proposed as the cause of hysteresis in some ferromagnetic III-V materials. However, the formation of Mn<sub>4</sub>N clusters does not influence the magnetization above 50K, since clearly the magnetization drops to zero at that

temperature. Also, the magnetization vs. temperature indicates that the formation of AlMn clusters is not the cause of the ferromagnetism observed, evidenced by the order of magnitude difference between the values of magnetization over 150K. Hence, the incorporation of Mn into the AlN lattice forming the ternary AlMnN is most likely the reason for the observed hysteresis.

In conclusion, room temperature ferromagnetism has been observed in AlMnN grown by gas-source MBE. The lattice constant decreased with increasing Mn cell temperature for single phase material, indicating constant site occupation, probably substitutional. Hysteresis in  $M$  vs.  $H$  at room temperature was observed in single phase material and the magnetization as a function of temperature suggests ferromagnetism caused by AlMnN, not clusters.

### **Growth of Thin Film AlCrN**

AlCrN films were grown by Molecular Beam Epitaxy (MBE) on c-plane sapphire in a similar fashion to the AlMnN films discussed in the previous section. The same Al and nitrogen sources were used, and the same nitridation, nucleation, and high temperature buffer layers were grown prior to DMS growth. Solid Cr (7N) was used as the dopant source in the AlCrN films by heating in a standard effusion cell. AlCrN films were grown at a substrate thermocouple temperature reading ( $T_s$ ) of 780°C. The AlCrN films were grown with a Cr cell temperature thermocouple reading ( $T_{Cr}$ ) from 982-1005°C. The Cr concentrations were in the range 1-3 at. %, as measured by x-ray microprobe and secondary ion mass spectrometry.

Reflection high energy electron diffraction (RHEED) was observed *in situ* and used to monitor the film growth. The AlCrN films for the most part demonstrated 3D growth, as evidenced by spotty RHEED patterns. However, the AlCrN grown at  $T_{Cr} = 982^\circ\text{C}$

demonstrated 2D growth with a pattern indicative of a 1x3 reconstruction (Figure 4.5), which was not observed for any other AlCrN films. Atomic force microscopy (AFM), a widely-used tool for investigating the topology of materials, was used to investigate the surface morphology of the AlCrN films. As expected from the RHEED patterns, the AlCrN films were considerably rougher than undoped AlN grown under similar conditions (Figure 4.6).

### Crystallinity and Phase Structure

Single phase and multi-phase AlCrN films were investigated. Powder x-ray diffraction was used to determine the phase composition of the films. The materials corresponding to  $T_{Cr} = 982-992^{\circ}\text{C}$  were found to be single phase while material grown at  $T_{Cr} = 1005^{\circ}\text{C}$  was found to contain multiple phases. Both  $\text{Cr}_2\text{N}$  and  $\text{Al}_x\text{Cr}_y$  (most likely corresponding to  $\text{Al}_3\text{Cr}_2$  and  $\text{AlCr}_3$ ) were found in the higher Cr content film. High resolution x-ray diffraction was used to determine the lattice constant of the AlCrN films. As shown in Table 4.1, the lattice constant ( $a_0$ ) of the single phase AlCrN was smaller than for AlN. This behavior was also observed in the similarly grown AlMnN films, as reported earlier in the chapter. The presence of second phases increased  $a_0$  relative to the single phase films. A decrease in lattice constant with the introduction of a dopant indicates substitutional incorporation of the dopant. The rise in lattice constant with the presence of multiple phases suggests that more of the dopant is incorporating interstitially. The single phase AlCrN was found to be semi-insulating, while the multi-phase material was found to conduct via an electron hopping mechanism with activation energy for conduction of 0.19 eV. For non-optimized growth, second phases of  $\text{Cr}_2\text{N}$  and  $\text{Al}_x\text{Cr}_y$  are produced in the AlN and the material is conducting ( $\sim 1000 \text{ Ohm-cm}$ ), see Table 4.1.

### **Role of V/III on Growth and Magnetic Properties**

The nitrogen flux was varied from 1.2-1.5 sccm in the growth of the AlCrN films to determine optimal V/III ratio. The significance of the V/III ratio lies in the relationship between incorporation of the transition metal ion and the resulting magnetization. Without a change in group III species or growth temperature, a change in group V species will affect the number of substitutional sites for dopants to occupy. At high V/III, however, the excess N at the surface may interfere with the transition metal incorporation, resulting in a reduction of the magnetic ordering. This results in an optimal V/III which will incorporate the maximum number of substitutional dopants. It follows that this will lead to the maximum magnetic signal arising from the substitutional dopants. Figure 4.7 shows the variation of the 300K saturation magnetization with respect to the flow rate of the nitrogen for the AlCrN films grown at  $T_{Cr} = 987^{\circ}\text{C}$ . High  $\text{N}_2$  flows appear to reduce the sticking coefficient of the Cr, resulting in a reduced Cr concentration and hence lower  $M_s$ .

### **Effect of Dopant on Ferromagnetism**

The ferromagnetic signal was found to be much stronger in the optimized AlCrN film than in the optimized AlMnN film. Figure 4.8 compares the magnetization vs. applied field for the optimal AlCrN and AlMnN films. The signal strength of the optimized AlCrN is  $\sim 2.5$  times that of the optimized AlMnN. This suggests that the ferromagnetic interaction in the AlN between the Cr ions is stronger than that of the Mn ions. The coercive fields of the AlCrN and AlMnN are nearly identical. This suggests that the domain structures of the materials are similar.

Strong ferromagnetism persists to 350K (the temperature limit of the SQUID magnetometer), in the optimized AlCrN. Moreover, the saturation magnetization remains



unchanged in the temperature region from 10K-350K. By contrast, AlMnN films grown under similar conditions were found to decrease in magnetization at 300K as compared to 100K, as shown in Figure 4.1. This suggests that AlCrN has a Curie point above that of AlMnN. Moreover, the Curie temperature of AlCrN is well above room temperature whereas the Curie temperature of AlMnN is in the vicinity of room temperature. Another difference between the AlMnN and the AlCrN is in the shape of the magnetization vs. temperature trace. Interestingly, the “paramagnetic tail” seen in the AlMnN in the 10-50K region is less pronounced in the single phase AlCrN, as shown in Figure 4.9. This may be another indication of a stronger ferromagnetic interaction between Cr dopant ions and Mn dopant ions. Overall, Cr tends to be a better dopant than Mn in ferromagnetic AlN.

Table 4.1. Table featuring the lattice constant and electrical properties of AlMnN and AlCrN films.

	Lattice Constant (Ang)	FWHM	Carrier Type/ Concentration (cm <sup>-3</sup> )	Resistivity ( $\Omega$ cm)
AlN	4.89592	0.0919	-	insulating
AlMnN (TMN=635° C)	4.89292	0.0928	-	-
AlMnN (TMN=650° C)	4.89169	0.0902	p-type/~1E18	1.6
AlMnN/Al Mn	4.89326	0.0984	n-type/~2E20	5.7E-3
AlCrN			-	-
AlCrN/Al <sub>x</sub> C r <sub>y</sub> +Cr <sub>2</sub> N				1000

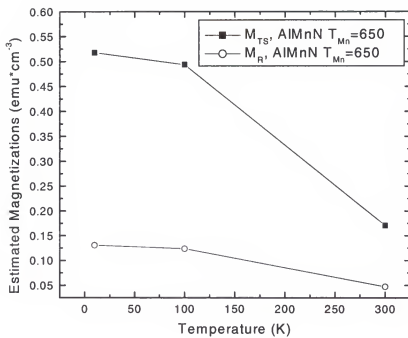


Figure 4.1. Estimated saturation magnetization and estimated remanent magnetization of AlMnN. The film was grown with Mn cell temperature of 650°C and under a nitrogen flow of 1.3 sccm.

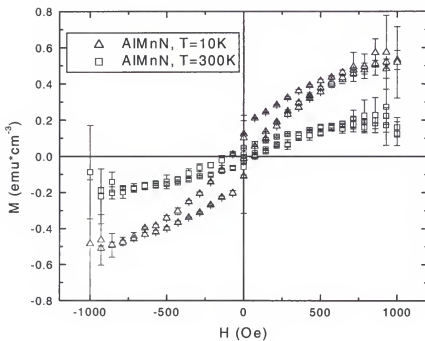


Figure 4.2. Magnetization versus applied magnetic field for AlMnN at temperatures of 10K and 300K. The film was grown with a Mn cell temperature of 650°C and under a nitrogen flow of 1.3 sccm.

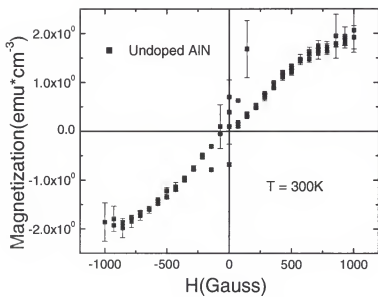


Figure 4.3. Magnetization vs. applied field of the undoped AlN showing paramagnetic behavior.

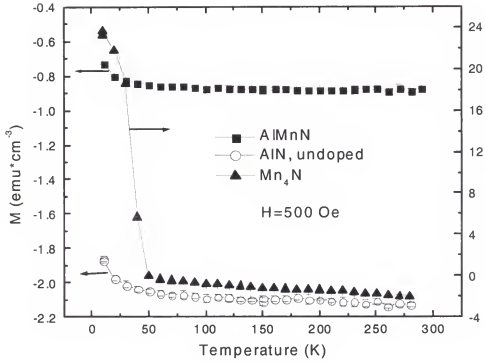


Figure 4.4. Magnetization versus temperature for films of either undoped AlN, single phase AlMnN, or  $Mn_4N$ .

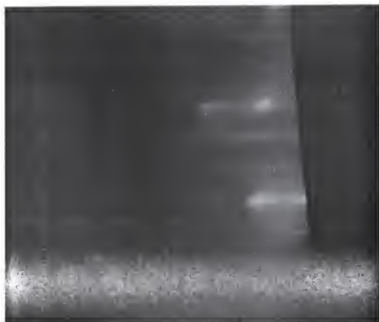


Figure 4.5. Reflection high energy electron diffraction photo of AlCrN film grown at a Cr cell temperature of 992°C. The photo depicts a 2D/3D pattern with one by three reconstruction.

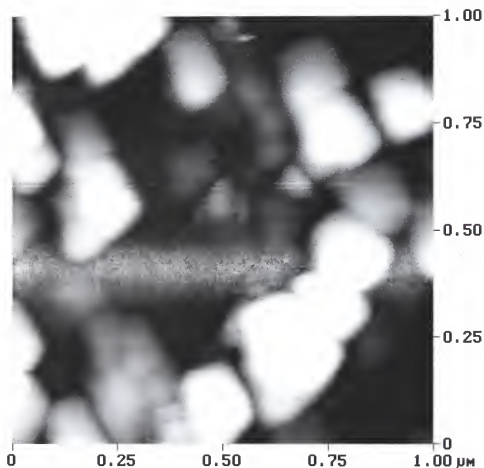


Figure 4.6. Atomic force microscopy image ( $1\mu\text{m}$  by  $1\mu\text{m}$ ) of AlCrN with an rms roughness value of approximately 11 nm.



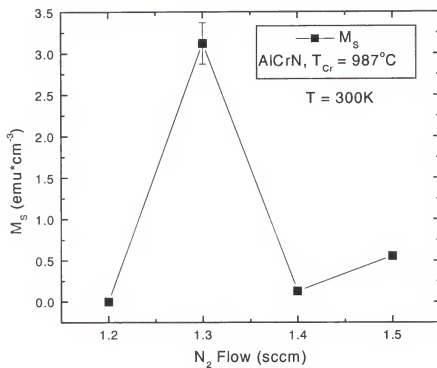


Figure 4.7. Magnetization versus nitrogen flow for AlCrN films grown at a substrate temperature of  $780^\circ\text{C}$  and with a Cr cell temperature of  $987^\circ\text{C}$ .

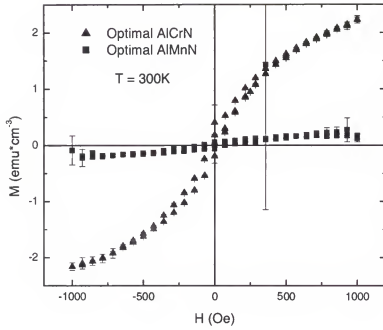


Figure 4.8. Magnetization vs. applied field for the optimal AlCrN and AlMnN films.

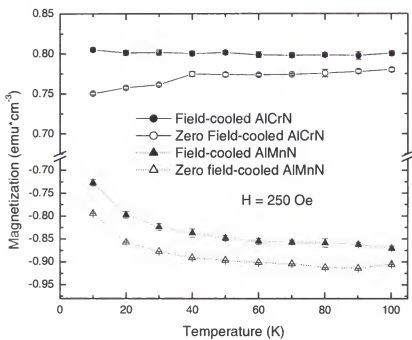


Figure 4.9. Magnetization vs. temperature in the temperature range from 10K-50K for AlMnN and AlCrN. A difference in curvature is seen for the two materials.

## CHAPTER 5

### THERMAL STABILITY INVESTIGATION

The prospects for integrating a dilute magnetic semiconductor (DMS) into current technology depend upon the ability for the material to withstand certain chemical, thermal, and mechanical processes that occur during the processing of the thin film material into devices. Typically, III-N semiconductors are exposed to chemicals, in the form of solvents such as methanol and isopropyl alcohol, during the fabrication of devices including high electron mobility transistors (HEMTs) and light emitting diodes (LEDs). Standard procedures utilizing solvents are performed to mask the underlying material in order to provide a particular pattern to either remove the semiconductor or to deposit metal contacts. The strong bonding found in the III-Ns made these DMS resistant to such chemical exposure. However, some of the metal contacts to the III-Ns require a heat-activating intermixing of various metal layers. This thermal anneal procedure is necessary to produce optimal electrical contact for III-N ohmics. Thermal anneal temperatures may easily exceed 700°C, or the low growth temperature required for III-N DMS growth. For this reason, it is necessary to investigate the thermal stability of DMS, to be certain that the material will withstand the elevated temperatures encountered during processing.

In order to effectively determine the material's thermal stability with respect to magnetic ordering, a systematic approach is applied. The magnetization of thin film epi-AlN DMS, is probed after a rapid thermal anneal at temperatures increasing in 100°C increments. The magnetization is extracted from SQUID measurements taken at 300K

after each rapid thermal anneal (RTA) until no hysteresis is observed. The RTA temperature at which the magnetization is lost is taken to be the upper thermal limit of the material. In this manner, the thermal stability of III-N DMS may be systematically studied.

The optimal epi-AlCrN used in the investigation of thermal stability was grown at a substrate temperature ( $T_s$ ) equal to 780°C with an Al cell temperature ( $T_{Al}$ ) of 1150°C and a Cr cell temperature ( $T_{Cr}$ ) of 987°C. The material was grown under a nitrogen plasma with a flow of 1.3 sccm. The AlCrN was annealed from 300°C-700°C in 100°C increments. Figure 5.1 shows the estimated saturation magnetization for each of the anneal temperatures. The estimated saturation magnetization was taken to be the magnetization at an applied field of 1000 Oe. From the as-grown condition (no anneal) to the initial anneal at 300°C, the magnetization decreases from 3.12 emu/cm<sup>3</sup> to 1.11 emu/cm<sup>3</sup>. This drastic drop by almost a third indicates that the magnetic ordering is being affected by even a low temperature anneal at 300°C. The magnetization then decreases at the subsequent anneal at 400°C, nearly an order of magnitude below the as-grown value, but remains stable until  $T_{\text{anneal}} = 700^\circ\text{C}$ . This indicates that the magnetic ordering is unaffected in the temperature range from 400°C up to nearly 700°C. However, at  $T_{\text{anneal}} = 700^\circ\text{C}$  nearly all magnetic ordering is lost, as shown in Figure 5.2. The raw magnetization vs. applied field ( $M$  vs.  $H$ ) after annealing at 700°C shows evidence of some hysteresis remaining, however the data is noisy and the loop is nearly flat implying that most of the magnetic ordering is destroyed by the 700°C anneal. The magnetization vs. temperature ( $M$  vs.  $T$ ) before and after the 700°C anneal (Figure 5.3) corroborates the observation that the magnetization is lost as compared to the as-grown AlCrN. The noisy,

yet consistently near zero, field-cooled signal is well below the signal obtained in the as-grown case.

The upper limit of thermal resistance to magnetic degradation of the epi-AlCrN appears to be very near, yet lower than, the growth temperature of the material. The apparent discrepancy between the temperature at which the material's magnetic properties degrade and that of the magnetic properties of the as-grown AlCrN is explained as follows. During growth, active nitrogen species are delivered to the surface which is at elevated temperatures. This exposure to the active nitrogen species continues after growth during the cool down of the material. This is routine procedure which prevents the disassociation of nitrogen from the material while the material is still heated, ultimately resulting in no change of material during cool-down. However, during the RTA, the ambient gas is  $N_2$ , not the atomic nitrogen found in the plasma. It is plausible that during the anneal the quality of the AlCrN degraded due to the elevation of temperature without an atomic nitrogen overpressure, which lead to the loss of nitrogen and degradation of magnetic ordering. The extent of degradation could range from slight deterioration in crystallinity of the AlCrN to destruction creation of second phases.

The investigation of the AlCrN material phase after the 700°C anneal would give a clear indication of phase degradation. Figure 5.4 shows the powder x-ray diffraction (XRD) scans of AlCrN before and after the anneal at 700°C. No second phases are observed after the 700°C anneal. The main difference between the XRD scans is the broad peak around 20 degrees, which corresponds to the substrate, and gives no insight into the epi layer. The absence of second phases implies that the extent of material degradation from the anneal is not sufficient enough to change the phase of the material.

However, as seen in the SQUID data, the effect of a 700°C anneal leads to a degradation of magnetic properties.

The thermal stability of optimal epi-AlCrN was investigated and was found to be poorer than that of GaCrN. The upper limit of anneal temperature before destruction of magnetic properties was found to be 700°C. No indication of second phases was observed after the 700°C anneal, which implies that the RTA was not significant enough to destroy the single phase AlCrN. However, although the single phase AlCrN withstood the RTA, the magnetic interaction within the material did not. This suggests that the mechanism for magnetization within this particular DMS is too weak to endure routine processing procedures during fabrication, such as the annealing of ohmic contacts. Hence, processing procedures must be altered for incorporation into current technology or alternate materials will need to be used in place of AlCrN.

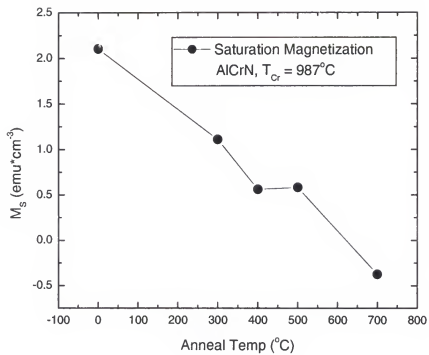


Figure 5.1. Estimated saturation magnetization for AlCrN at each anneal temperature.



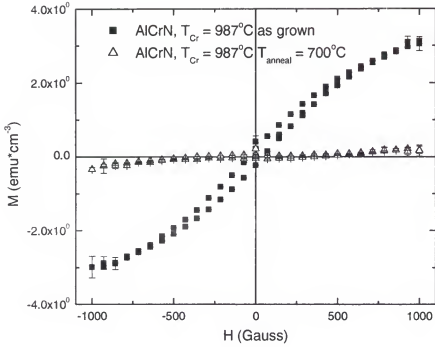


Figure 5.2. Magnetization versus applied field measurements comparing the as-grown AlCrN to the post-anneal AlCrN. Very little magnetization is left after an anneal of the AlCrN at  $700^\circ\text{C}$ .

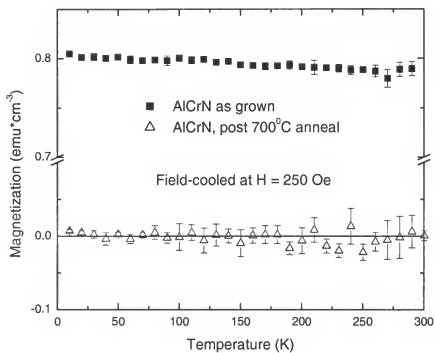


Figure 5.3. Magnetization versus temperature taken under an applied field of 250 Oe comparing as grown AlCrN to post-anneal AlCrN.

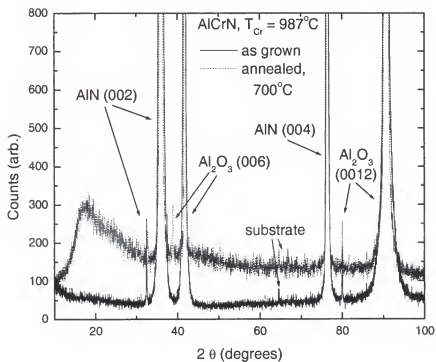


Figure 5.4. Powder x-ray diffraction scans comparing as grown AlCrN to post-annealed AlCrN. No second phases are apparent after the 700°C anneal.

## CHAPTER 6

### ALN AND GAN BASED DILUTE MAGNETIC SEMICONDUCTOR APPLICATIONS

#### **Spin Filter Applications of AlN DMS**

The most obvious application of an AlN-based DMS into an active device is by its use as a ferromagnetic barrier. A ferromagnetic insulator shows promise as a spin filter by allowing tunneling of aligned electrons and preventing tunneling of antiparallel electrons. The effect is a change in resistance with applied magnetic field and is dubbed tunneling magneto-resistance (TMR). For example, EuS was used as a spin filter and showed evidence of magnetoresistance (MR) exceeding 130% at temperatures below the Curie temperature of the material (~70K). AlN has the potential of being applied in the same manner, however with an operable device at room temperature, since the Curie point is above 300K.

#### **Device Structure and Design**

The all semiconductor device structure schematic is shown in Figure 6.1. Two device stacks were grown, one with a ferromagnetic insulator and a reference with a non ferromagnetic insulator. The tunneling magneto-resistance (TMR) stack includes two ferromagnetic layers: a spin injector which serves to provide electrons with aligned spin states and a spin filter which controls the amount of charge transport via tunneling. The reference stack contains only one ferromagnetic layer, the spin injector. In the case of the TMR stack, tunneling is expected to increase if both the spin injector and spin filter are magnetically aligned by the application of an external magnetic field. However, in the

case of the reference device, there is no change expected in tunneling with the application of an external magnetic field.

In the TMR stack, optimal GaMnN was used as a spin injector and optimal AlMnN was used as a spin filter. In the reference stack, the AlN was grown under the same conditions as the TMR stack, but without the addition of Mn. Both structures were grown on an MOCVD-GaN buffer from the same wafer, which was chemically pretreated with a 3 minute 1:1 HCl:H<sub>2</sub>O dip, a 25 minute UVO<sub>3</sub> exposure, and a 5 minute BOE dip followed by a DI rinse and N<sub>2</sub> dry. The substrate was heated in situ under N plasma to 700°C before growth and a streaky RHEED pattern was obtained prior to growth to ensure a clean growth surface. A 50 nm thick GaN:Si layer was grown, followed by a 7.5 nm AlMnN layer (AlN, for the reference stack). The GaMnN spin injector was 10 nm thick and another 50 nm GaN:Si layer was grown to provide better electrical contact to the ohmics.

The devices were then fabricated into thin bars with large area contact pads on each end. The mask design is shown in Figure 6.3. The bar bell type structures allow for incorporation of anisotropic ferromagnets such as Co, for which the aspect ratio of 10:1 would force the coercive field to higher values. This shape is useful for creating large differences in the values of the coercive fields to separate magneto-resistance maxima in measurements. The devices were fabricated using standard photolithography to pattern and etch mesas via ICP and to pattern then evaporate ohmic contacts. An SEM image of the fabricated all semiconductor TMR device is shown in Fig. 6.4. Ohmic contacts consisted of 50 nm Ti and 500 nm Au. Ohmic contacts were not annealed to improve

contact resistance due to the thermal instability of the DMS, which is addressed in Chapter 5.

### **Device Testing and Results**

Electrical and magneto-resistance measurements were performed to determine the functionality of the devices. All measurements were done on both the TMR stacks and the reference stack. Room temperature current-voltage (I-V) measurements of the TMR stack without an applied magnetic field and with an applied magnetic field compare device operation in the randomized state vs. device operation in the parallel state. Figure 6.5 shows an increase in slope and exponential behavior of the TMR device after an applied field of  $H = 4000$  Oe. The device in the randomized state shows less of the expected tunneling behavior (as indicated by the decrease in slope). This suggests that the tunneling increases when the GaMnN and AlMnN are aligned, which agrees with the expected operation of the device. The room temperature I-V measurements provide a useful survey method to determine the promise of the device.

Magneto-resistance (MR) measurements were performed in a Quantum Design Physical Properties Measurement System (PPMS) by measuring the resistance of the samples while sweeping an applied magnetic field. The PPMS measurements are limited to a maximum of 95 mV and  $999\mu\text{A}$ . These restrictions hinder measurements of highly resistive material. The room temperature measurement of the reference sample showed no change in resistance with respect to the magnetic field. This complies with the expected behavior with no spin filter. The resistance vs. applied magnetic field (R vs. H) at 5K is shown in Figure 6.6 for the reference device. A slight change in resistance appears at high field, which most likely comes from the small change in resistance of the GaMnN. Since the change is so small, it is most likely due to the thin spin injector's

inherent magnetoresistance. The origin of the splitting of resistances between 3000 Oe to -500 Oe and on the up sweep between -500 Oe to 3000 Oe is unknown. However, the same splitting is found in the  $R$  vs.  $H$  of the TMR device at 300K, shown in Figure 6.7. No MR can be seen at 300K in the TMR device. Comparison measurements at 5K could not be performed due to the high contact resistance found in the TMR device at low temperature.

Structural investigation of the TMR device was performed by TEM of the cross section of the device to determine the growth quality at the interfaces. Fig. 6.8 is a dark field image where the TRM layers can easily be seen. Interfacial roughness between the GaN:Si and the AlMnN layer is evident by the wave-like shape of the AlMnN layer. Upon closer examination of the AlMnN layer, defects can be seen (Fig. 6.9). This indicates that the growth of the device is not optimized, and is a plausible reason for the inability of the device to operate as expected at room temperature.

In conclusion, room temperature I-V measurements showed promising results for the TMR device. Tunneling increased when the spin injector and spin filter were aligned, as compared to the randomized state. However, PPMS measurements were not quite so promising, in that no TMR was observed at room temperature in the TMR device. Unfortunately, due to the limits of the PPMS, no MR measurements could be made at low temperature. Through TEM imaging, high amounts of strain were observed in the AlMnN spin filter. This is one possible reason for no MR at 300K. Another possibility is that the Mn impurity introduces impurity bands into the DMS (as discussed in Chapter 4). This distribution of levels may cause the MR to be less defined.

Other spin injectors were also grown, namely FeNi and MnAs, which replaced the GaMnN in the TMR stack. FeNi did not withstand the photolithography, and oxidized and degraded before testing was accomplished, see Figure 6.10. The MnAs survived processing, but was too soft for wire bonding, making MR measurements impossible. Improvements on TMR devices can be made by using alternative tunnel layers which contain an impurity level instead of impurity distribution. One such promising impurity is Gd, which would allow for a single impurity level in III-N DMS.



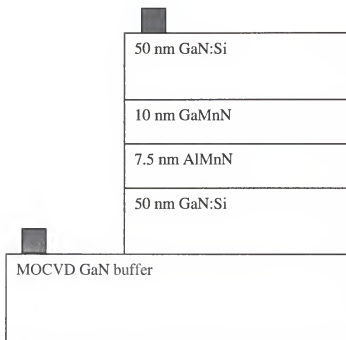


Figure 6.1. Schematic of the all semiconductor tunneling magneto-resistance stack. The reference stack contained undoped AlN in place of the AlMnN layer, and all thicknesses remained the same. The dark squares represent ohmic contacts made to the top GaN:Si layer and to the underlying MOCVD GaN buffer.

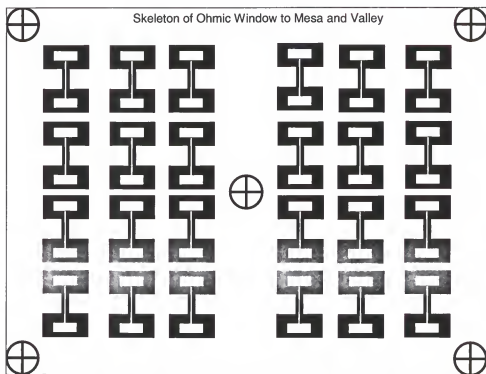


Figure 6.3. Mask design used for fabrication of all semiconductor device. Alignment marks are found at each corner and in the middle of the mask. The larger dark bars represent the area of the mesa of the device. The open, or light areas, represent where ohmic contact was made to the device.

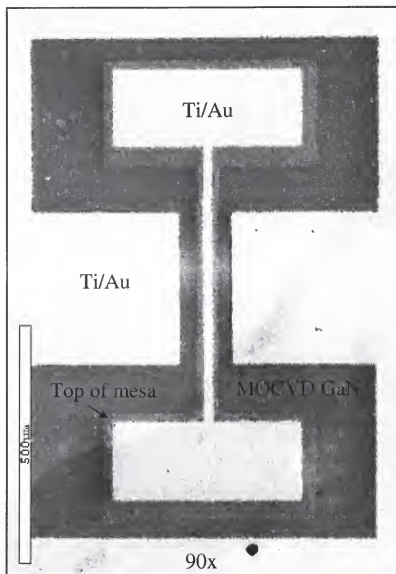


Figure 6.4. Scanning electron micrograph of all semiconductor device. Top view shows top and bottom Ti/Au ohmic contact, the top of the mesa and the etched valley showing the MOCVD GaN buffer.

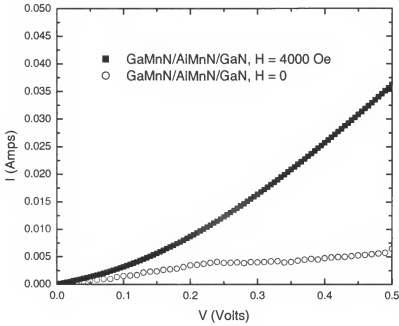


Figure 6.5. Current-voltage measurement of all semiconductor tunneling magnetoresistance device with and without and applied magnetic field. Open circles represent the I-V measurement taken without an applied field. Dark squares represent I-V measurement taken after application of a 4000 Oe field. Note that tunneling increases after the field is applied.

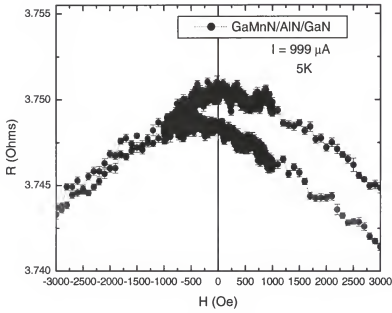


Figure 6.6. Resistance vs. applied field measurement taken at 5K for the all semiconductor reference device.

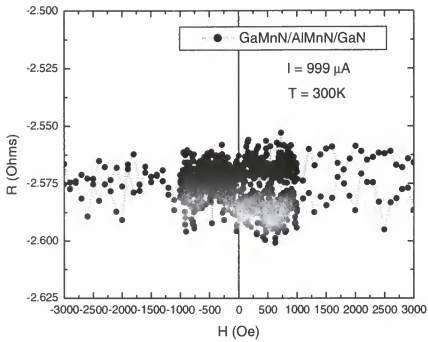


Figure 6.7. Resistance vs. applied field taken at 300K for the all semiconductor tunneling magneto-resistance device.

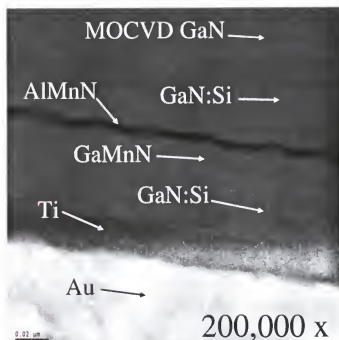


Figure 6.8. Dark field ZSTEM image taken of the all semiconductor tunneling magnetoresistance device. The dark AlMnN layer shows roughness indicating poor growth quality at the interface.

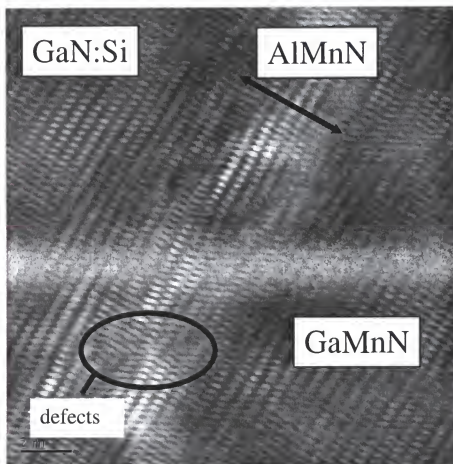


Figure 6.9. Selected area diffraction pattern tunneling electron micrograph taken of the all semiconductor tunneling magneto-resistance device. The AlMnN spin filter layer is indicated with an arrow. Strain can be seen within the AlMnN layer as indicated in the photo.





Figure 6.10. Scanning electron micrograph of a tunneling magneto-resistance device with FeNi as a spin injector. From the photo, the degradation of the FeNi is visible on the contact pad. This degradation represents nearly 90% of the devices. The FeNi degraded during photolithography, most likely due to the use of solvents during processing.

## CHAPTER 7 INVESTIGATION OF GADOLINIUM AS A MAGNETIC DOPANT

### Introduction of a New Magnetic Dopant

The incorporation of transition metals (such as Mn and Cr) into III-Ns results in ferromagnetic semiconductors. However, as discussed in previous chapters, the resulting DMS is not optimal for incorporation into devices. Very recently, another potential dopant for III-Ns has been reported.<sup>39</sup> A large magnetic moment was found for GaN:Gd. The strong ferromagnetism arose from a low concentration level ( $<10^{16} \text{ cm}^{-3}$ ) of Gd in GaN. This was attributed to a long range spin polarization of the Gd atoms within the GaN. The importance of this finding lies in the ability to dope a DMS with carriers of a concentration greater than the Gd concentration.<sup>39</sup> Therefore, it is possible to effectively utilize GaN:Gd in spintronic devices without relying on an impurity band or pinning the Fermi level within the DMS. For this reason, the magnetic properties of epitaxial GaN doped with Gd are explored.

### Growth of GaN:Gd

Epitaxial GaN doped with Gd was grown by gas source molecular beam epitaxy (GSMBE). Samples were grown on metalorganic chemical vapor deposition (MOCVD) GaN buffers, chemically treated prior to growth with the standard preparation discussed in Chapter 4. The substrates were heated to 700°C under 1.6 sccm nitrogen plasma before growth to verify a streaky reflection high energy electron diffraction (RHEED) pattern, which indicates a clean growth surface. During growth initiation, the substrates were first exposed to Ga and N, before the Gd shutter was opened. Each of the GaN:Gd

samples was grown at a substrate thermocouple reading ( $T_s$ ) of 700°C, a Ga cell temperature ( $T_{Ga}$ ) of 785°C and a nitrogen plasma flow of 1.6 sccm. The Gd cell temperature ( $T_{Gd}$ ) was varied between 900°C-1125°C.

RHEED was used to monitor the growth in situ. Samples corresponding to  $T_{Gd} = 900$ -950°C demonstrated spotty (3D) RHEED patterns. GaN:Gd grown at  $T_{Gd} = 1050$ °C demonstrated 2D/3D RHEED patterns with a 1x3 reconstruction. Figure 7.1 shows the 1x3 reconstruction observed during growth of the GaN:Gd. Atomic force microscopy (AFM) was used to investigate the roughness of the films after growth. An AFM image of Gd-doped GaN is shown in Figure 7.2 for  $T_{Gd} = 950$ °C. The rms roughness value was 2.934 nm, which was typical for all GaN:Gd.

### **Magnetic Properties of GaN:Gd**

Superconducting quantum interference device (SQUID) magnetometry was carried out in a Quantum Design Magnetic Properties Measurement System (MPMS) to investigate the magnetic behavior of the GaN:Gd. Background magnetization was subtracted out as described in the appendix.

Magnetization vs. applied field (M vs. H) was scanned for each of the GaN:Gd samples. For  $T_{Gd} = 900$ °C, no hysteresis was observed at any temperature. At  $T_{Gd} = 950$ °C, ferromagnetism is observed at 50K, as shown in Figure 7.3. However, the magnetization level is very low at 50K and becomes noisy and questionable at 300K and 350K. For  $T_{Gd}$  in the range of 1000°C-1100°C, ferromagnetism is clearly evident in the M vs. H loops. Figure 7.4 shows the M vs. H loops at 50K for the samples corresponding to  $T_{Gd} = 1000$ -1100°C. At  $T_{Gd} = 1125$ °C, there is no evidence of ferromagnetism in GaN:Gd at 50K, 300K, or 350K. Therefore, the Gd cell temperature range of 100°C yields ferromagnetism in GaN:Gd.

A comparison of the estimated saturation magnetization (corresponding to the magnetization at 1600 Gauss) depicts the dependence of ferromagnetism on  $T_{\text{Gd}}$ . The optimal Gd condition is  $T_{\text{Gd}} = 1050^\circ\text{C}$ , as shown in Figure 7.5. This trace of  $M_S$  and  $M_R$  at 300K vs.  $T_{\text{Gd}}$  implies that there is a certain amount of dopant which yields the maximum magnetization. This behavior is similar to that found for the transition metal dopants, Mn and Cr, as discussed in Chapter 4. However, unlike the transition metal dopants, the Gd incorporation is at a much lower level. The flux readings for Mn and Cr during growth are on the order of  $10^{-8}$ , but the Gd flux reading is much lower, below  $10^{-10}$ . The presence of an optimal cell temperature for the transition metals can be attributed to the concentration level and incorporation site of the dopants. At too low of a cell temperature, not enough dopant is incorporating substitutionally which results in a low magnetization level. At too high a cell temperature (corresponding to a few atomic percent dopant) the transition metals begin to occupy interstitial sites which results in a degradation of the magnetic interaction. However, in the case of Gd, it is not probable that the amount of Gd incorporated into the GaN can be high enough for the Gd to incorporate interstitially. Therefore, a different mechanism must be driving the magnetization in GaN:Gd.

The magnetization vs. applied field for  $T_{\text{Gd}} = 950^\circ\text{C}$  was found to decrease from 50K to 350K. However, this behavior was not observed at higher  $T_{\text{Gd}}$ . Figure 7.6 shows the M vs. H loops at  $T = 50\text{K}$ ,  $300\text{K}$ , and  $350\text{K}$  for  $T_{\text{Gd}} = 1050^\circ\text{C}$ . The magnetization appears stable from 50K to 350K for  $T_{\text{Gd}} = 1050^\circ\text{C}$  as indicated by the loops. However, the magnetization vs. temperature (M vs. T) seems to indicate a decrease in magnetization, as shown in Figure 7.7. The zero field-cooled and field-cooled traces are

widely separated until near room temperature. The instability around room temperature may be a sign that this temperature is in the vicinity of the Curie point ( $T_C$ ) of the material. This behavior is reminiscent of that of bulk Gd, which has a  $T_C \sim 300\text{K}$ . Conversely, the magnetization of the transition metals (which are antiferromagnetic) do not correspond to the magnetization in III-N:TM. This is yet another indication that there is a different mechanism of ferromagnetism in the GaN:Gd.

### Thermal Stability Investigation of GaN:Gd

As described in detail in Chapter 5, the thermal stability of the optimal GaN:Gd ( $T_{\text{Gd}} = 1050^\circ\text{C}$ ) was investigated in a systematic way. The GaN:Gd was annealed from  $300^\circ\text{C}$  to  $700^\circ\text{C}$  to determine the temperature at which magnetization is destroyed.  $M$  vs.  $H$  measurements taken at  $300\text{K}$  for each anneal temperature indicate the change in magnetization with anneal temperature. Figure 7.8 shows the saturation magnetization vs. the anneal temperature ( $T_{\text{anneal}}$ ). After the first anneal at  $300^\circ\text{C}$  the saturation magnetization immediately decreases from the as grown value and generally decreases as the anneal temperature increases. This is a possible indication of the destruction of the magnetic properties of the film. However, the  $M$  vs.  $H$  depicts a different scenario. Figure 7.9 compares the  $M$  vs.  $H$  of the as grown GaN:Gd to that annealed at  $600^\circ\text{C}$ . As shown in figure 7.8, the saturation magnetization decreases by a factor of greater than one half. Although the maximum magnetic signal decreases, the overall hysteresis increases. The loop becomes more square, with an increase in magnetic remanence and coercivity. This broadening of the remanence and coercivity indicates a “hardening” of the ferromagnetism. One possible explanation of the hardening involves a change in domain structure. The high anneal temperature may alter the domain structure in such a way as to make the domains less easy to manipulate, thereby requiring a stronger magnetic field to

produce zero magnetization. The increase in remanence with anneal temperature indicates the retention of more magnetic alignment within the material. Therefore, it seems plausible that annealing the GaN:Gd creates an alteration within the domain structure producing a larger coercivity and remanence. Also, the decrease in saturation magnetization indicates a decrease in the strength of the magnetic interactions within the GaN:Gd, however the magnetization remains even after a 700°C anneal. This retention of magnetization after a high temperature anneal is an improvement in thermal stability compared to the Cr-doped AlN.

The M vs. T corroborates the existence of magnetism after the 700°C anneal. Figure 7.10 shows the separation in the field-cooled and zero field-cooled loops up to about 320K. Above 320K, the M vs. T suggests the magnetization is reduced greatly. This is also seen in the M vs. H at 350K as compared to 50K, shown in Figure 7.11. The overall hysteresis is decreased at 350K, with a lower coercivity and field at which the material saturates. Although the hysteresis is beginning to vanish at 350K, the GaN:Gd annealed at 700°C remains ferromagnetic at 300K, as shown in Figure 7.12. This result was not found for the material doped with transition metals, as discussed in Chapter 5. This suggests that the magnetic interaction within the GaN:Gd is not destroyed after a high temperature anneal. Moreover, it implies that Gd is a superior dopant to the transition metals.

The incorporation of Gd into GaN results in an overall improvement of magnetic properties. The magnetization is increased although the dopant concentration is lower. More importantly, the ferromagnetism persists even after a 700°C anneal. This results in the possibility of incorporating GaN:Gd into spintronic devices which require a high

temperature anneal without destroying the magnetic properties. The application of GaN:Gd into spintronic devices will rely on other material characteristics such as transport, which will require investigation. Also, the impact of Gd on conductivity requires further investigation. One possible method is to use current-voltage measurements to probe the impurity within a quantum well. This should show whether the impurity is a distribution of levels or a single level. Although more investigation is needed to probe the effectiveness of GaN:Gd, the initial findings suggest it is superior to other III-N DMS.

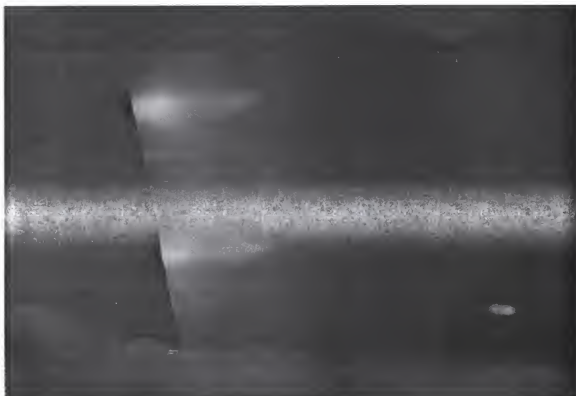


Figure 7.1. Reflection high energy electron diffraction pattern of GaN:Gd,  $T_{\text{Gd}} = 1050^{\circ}\text{C}$ . The picture shows a 2D/3D pattern with 1x3 reconstruction.



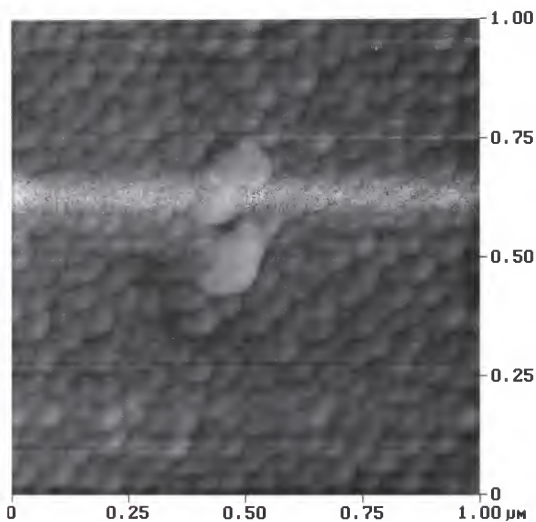


Figure 7.2. Atomic force microscopy image representing GaN:Gd with rms roughness of 1.541 nm.

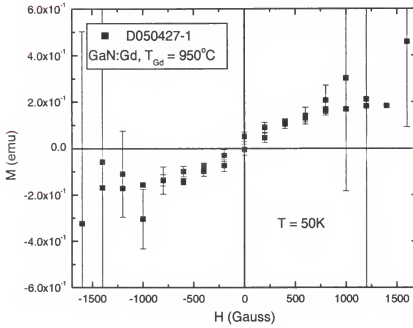


Figure 7.3. Magnetization vs. applied field loop taken at 50K for GaN:Gd, with  $T_{Gd} = 950^\circ\text{C}$ . Hysteresis is observed at 50K, but not necessarily at 300K or 350K.

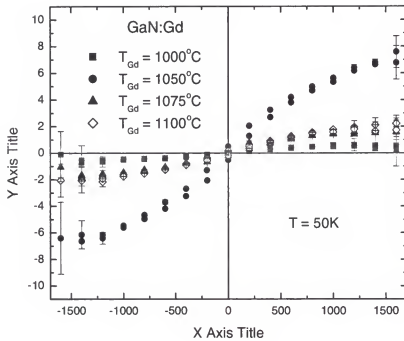


Figure 7.4. Magnetization vs. applied field taken at 50K for GaN:Gd corresponding to  $T_{\text{Gd}} = 1000^\circ\text{C}$ - $1100^\circ\text{C}$ .

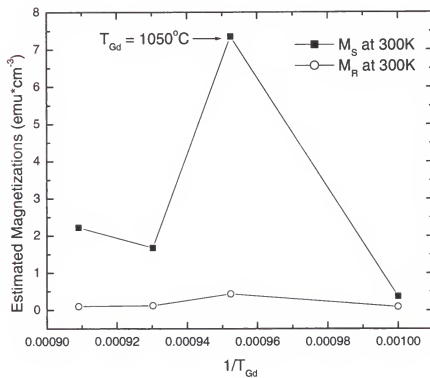


Figure 7.5. Estimated saturation magnetization vs. inverse of Gd cell temperature plot which shows the optimal T<sub>Gd</sub>.

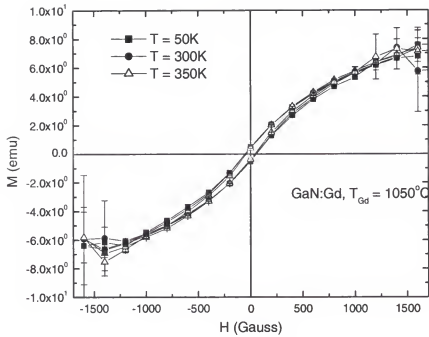


Figure 7.6. Magnetization vs. applied field loops taken at 50K, 300K, and 350K for GaN:Gd with  $T_{\text{Gd}} = 1050^\circ\text{C}$ .

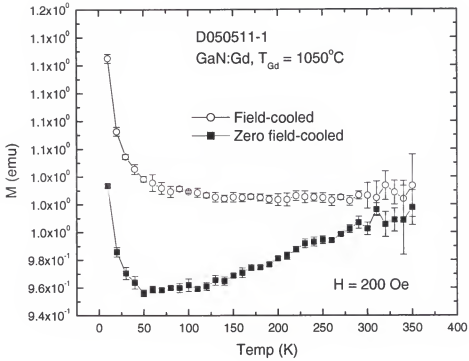


Figure 7.7. Magnetization vs. temperature for GaN:Gd with  $T_{\text{Gd}} = 1050^{\circ}\text{C}$ . Note that the magnetization is significantly decreased near room temperature.

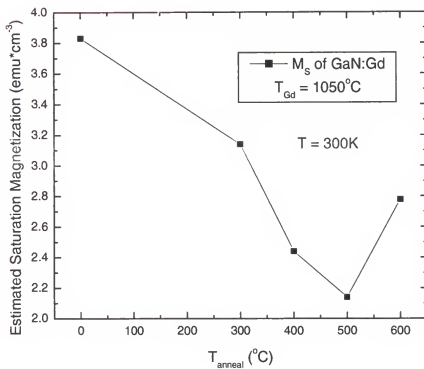


Figure 7.8. Estimated saturation magnetization vs. anneal temperature for GaN:Gd with  $T_{\text{Gd}} = 1050^{\circ}\text{C}$ .

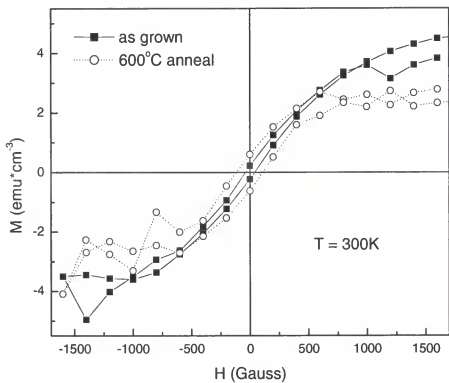


Figure 7.9. Magnetization vs. applied field comparing the as grown GaN:Gd to that annealed at 600°C.



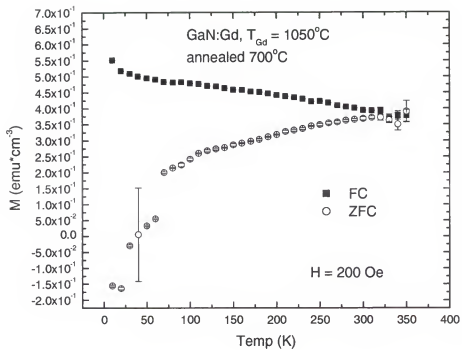


Figure 7.10. Magnetization vs. temperature of GaN:Gd after  $700^{\circ}\text{C}$  anneal.

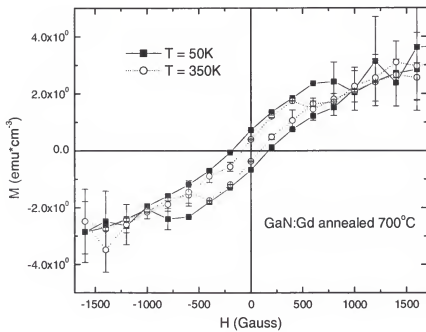


Figure 7.11. Magnetization vs. applied field at 50K and 350K for GaN:Gd annealed at  $700^\circ\text{C}$ .

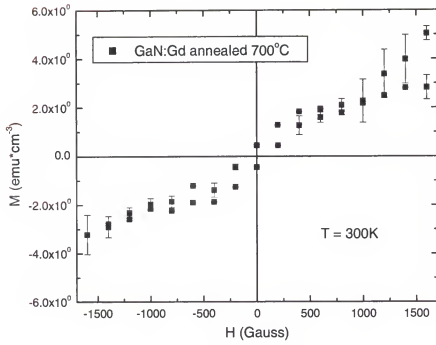


Figure 7.12. Magnetization vs. applied field at 300K for GaN:Gd annealed at  $700^\circ\text{C}$ .

## CHAPTER 8 CONCLUSION

The potential technological importance of dilute magnetic semiconductors ranges from an additional degree of freedom within a device to allow a multifunctional chip and the distant goal of quantum computing. However, in order to realize such possibilities, a few requirements must be met.

The most fundamental responsibility of the dilute magnetic semiconductor (DMS) is to exhibit ferromagnetism in thin film form. This provides evidence that the material has potential function within DMS-based device prospects. The ferromagnetism must exist at or beyond room temperature in order for the DMS to operate efficiently within current technology. Another requirement which must be met is that the DMS be stable against high temperatures which are found during the processing and fabrication of devices. This is an obvious requirement since the destruction of the DMS during fabrication into a device would lead to the inability of the fully fabricated device to operate. The more obscure requirements arise during the application of the DMS into currently used device schemes. For example, active devices (devices which depend on electron movement through the material) normally utilize single energy levels within a given layer of the device. These issues with respect to the effectiveness of AlN as a DMS have been addressed and are summed up in the following paragraphs.

### **AlN-based DMS Survey**

Three dopants, namely Mn, Cr, and Co, were surveyed as effective magnetic impurities in AlN by ion implantation. This is a quick method to incorporate a

predetermined amount of impurity and determine the plausibility of a given DMS. AlN substrates, grown by metal organic vapor deposition, were implanted with approximately three atomic percent of each impurity ion. Powder x-ray diffraction showed that the Mn-implanted AlN was single phase; however, both the Cr- and Co-implanted AlN exhibited second phases. Superconducting quantum interference device magnetometry showed that the single phase Mn-implanted AlN exhibited ferromagnetism at temperatures below 300K. Both the Cr- and Co-implanted AlN exhibited ferromagnetism at 300K. The additional phases found in the Cr- and Co-implanted material do not contribute to the ferromagnetic signal at 300K since the phases themselves are not ferromagnetic. In general, the use of ion implantation to introduce magnetic dopants into AlN suggests that Cr and Co ions are more magnetically active than Mn ions. However, Mn is more readily incorporated into AlN to produce single phase material. For these reasons, epitaxial AlMnN and AlCrN were investigated.

### **Impurity Comparison**

Two AlN-based DMS were grown by molecular beam epitaxy. The two different magnetic impurities introduced into the AlN host lattice were Mn and Cr, and the magnetic properties were investigated to determine the optimal dopant. The impurity cell temperature and the V/III were varied for both epitaxial AlCrN and AlMnN to optimize the magnetic signal. Both the AlMnN and AlCrN were ferromagnetic at room temperature. However, the magnetic signal versus applied field of the AlMnN decreased by a factor of 2 from 100K to 300K. The magnetic signal of the AlCrN showed no evidence of lessening over the same temperature range. It is possible that the Curie temperature of the AlMnN is lower than that of the AlCrN. Also, the magnetization of the

AlMnN was overall smaller than that of the AlCrN. This suggests that Cr is a better magnetic impurity than Mn in an AlN-based DMS.

### **Thermal Instability**

In order to determine the thermal stability of the AlCrN in an environment similar to that encountered during device processing, the film was thermally annealed in a systematic way. The magnetization of the AlCrN was found to decrease by almost one-third after a fairly low temperature anneal at 300°C. The magnetization was nearly completely destroyed by an anneal at 700°C. A very small amount of hysteresis remained, but the magnetization was nearly equal to zero. The AlCrN showed no evidence of second phases after being annealed, which suggests that the magnetization was not destroyed due to the formation of nonmagnetic phases. Most likely, the magnetic interaction between the impurities was destroyed by the 700°C anneal.

### **Device Applications**

The AlMnN was incorporated into an all-semiconductor tunneling magnetoresistance structure. The device was designed so that the resistance would decrease when the magnetization of the two ferromagnetic semiconducting layers was aligned. However, the device was found to demonstrate no dependence of resistance on magnetic field. It is possible that current limitations of the measurement system are responsible for the lack of resistance response to the applied field. However, it is likely that the distribution of levels available for tunneling created a passageway for electrons which does not depend strictly on magnetic field. Therefore, the impurity band would desensitize the magnetoresistance and prevent the device from operating in the expected manner.

### Summary and Future Work

Although the Cr was found to be a better magnetic dopant than the Mn in AlN, it was determined that neither Cr nor Mn are viable impurities for an AlN-based DMS. The incorporation of such a DMS into current technology is prevented by two things. The AlCrN is unable to withstand the high temperatures encountered during the processing of devices. Also, the introduction of one-three atomic percent of an impurity such as Mn or Cr introduces an impurity band into the semiconductor. This proves to be detrimental to an active device which relies on the transport of carriers through a single impurity level, not a distribution of impurity levels. Therefore, an alternative magnetic impurity should be investigated.

One such potential dopant includes Gd. It is possible to incorporate less than an atomic percent of Gd into a host semiconductor lattice. Therefore, Gd would act as a “true” dopant by introducing a single impurity level. If the incorporation of Gd into AlN results in ferromagnetism at room temperature, then it would be possible to incorporate an AlN-based DMS into an active device and potentially into current technology.

Initial investigations of GaN:Gd grown by gas source molecular beam epitaxy indicate that the material is ferromagnetic at room temperature. Also, the ferromagnetism appears to resist thermal anneals at 700°C. A quantum well consisting of 2.5 nm GaN:Gd layers separated by 10nm AlN spacer layers has been grown to determine the impurity level associated with the Gd dopant. The viability of Gd-doped III-N DMS rests in the proof that Gd introduces a single impurity level. This would allow the incorporation of the DMS into current semiconductor technology and would prove the capability of spintronics.

## APPENDIX

### SUPERCONDUCTING QUANTUM INTERFERENCE DEVICE MAGNETOMETRY

Magnetization measurements were performed in a Quantum Design's Magnetic Properties Measurement System which uses a superconducting quantum interference device (SQUID) to provide the capability to sense the magnetic moment of materials under investigation. The SQUID consists of two Josephson junctions in a closed superconducting loop, which allows the SQUID to detect extraordinarily small changes in external magnetic fields. The SQUID itself does not directly sense the magnetic moments of the material under investigation. The movement of the sample through superconducting rings that are connected to the SQUID with superconducting wires induces a current through the detection coils. The change of magnetic flux through the superconducting rings results in a change in electrical current which is proportional to the change in magnetic flux. The superconducting rings are inductively coupled to the SQUID detector, and therefore the change in the current through the rings alters the SQUID output voltage which is proportional to the magnetic moment of the material under investigation. The SQUID magnetometer is routinely calibrated with a Palladium sample of known mass. The SQUID is sensitive to very small current variations in the superconducting coils which allows measurement of samples with very small magnetic moments. This is the most sensitive of the magnetometry techniques, which is useful in investigating dilute magnetic semiconductors with very low magnetic moments.



### **Sample Measurement Method**

Typically samples are measured within a plastic drinking straw (by suggestion of the SQUID manufacturer, Quantum Design). The plastic straw is not known to have ferromagnetic signal associated with it. However, there is a small signal (mostly diamagnetic) which arises due to both the straw and also the substrate. This signal is subtracted as explained in the next paragraph. The general size of each sample measured in the SQUID is less than one centimeter squared. The sample is situated in the straw perfectly parallel to the straw so that the magnetic signal parallel to the sample is measured. The sample is centered with respect to the coils prior to measuring the magnetization vs. field or temperature. Also, the magnet itself is degaussed prior to measurement to ensure that no trapped magnetic flux remains in the magnet. Zero field cooled (ZFC) traces were performed by cooling the sample to 10K then applying a small magnetic field before sweeping the temperature. Field cooled (FC) measurements were performed by cooling the sample to 10K under a small applied field then sweeping the temperature. The net result of the zero field cooled and field cooled measurement is the determination of the temperature range over which irreversibility in the magnetization exists. In other words, determining the temperature over which the sample remains ferromagnetic. This range of irreversibility can also be seen by performing  $M$  vs.  $H$  loops at varying temperature. Both measurements together provide sufficient evidence to the type of magnetization of the material. If both hysteresis in the  $M$  vs.  $H$  loop and a difference in the FC and ZFC traces can be observed, then the material is deemed ferromagnetic.

### **Background Subtraction**

Another important aspect of the magnetization measurements is the subtraction of the background magnetization. The step is performed for each of the measurements (magnetization vs. applied field, or  $M$  vs.  $H$ ) to eliminate any extraneous magnetic signal. At the end of the  $M$  vs.  $H$  loop, the magnet is swept from 1 Tesla (T) to 5T to bring out the weaker diamagnetic and paramagnetic signals within the sample and sample holder. The slope of this high field sweep is the susceptibility of the background magnetization. The susceptibility multiplied by the magnetic field is then subtracted from the raw data. This is the method used to subtract the background magnetization.

## LIST OF REFERENCES

1. Wolf, Stuart A., J. of Superconductivity: Incorporating Novel Magnetism **13**, 195-199 (2000)
2. Das Sarma, S., American Scientist **89**, 516-523 Nov.-Dec. (2001)
3. Zorpette, G., IEEE Spectrum December (2001) 30-35
4. J. Gregg, W. Allen, N. Viart, R. Kirschman, C. Sirisathitkul, J-P. Schille, M. Gester, S. Thompson, P. Sparks, V. Da Costa, K. Ounadjela, M. Skvarla, J. of Mag. and Mag. Mat. **175**, 1-9 (1997)
5. J. L. Simonds, Physics Today 26-32 April (1995)
6. S. Wolf, D. Treger, IEEE Transactions on Magnetics **36** 2748-2751 (2000)
7. S. Das Sarma, J. Fabian, X. Hu, I. Zutic, Sol. St. Comm. **119** 207-215 (2001)
8. N. F. Mott, Proc. R. Soc. **153** 633 (1936)
9. M. Oestrich, J. Hubner, D. Hagele, P. J. Klar, W. Heimbrodt, W. W. Ruhle, D. E. Ashenford, B. Lunn, Appl. Phys. Lett. **74** 1251-1253 (1999)
10. G. Prinz, Physics Today 58-63 April (1995)
11. D. D. Awschalom, J. M. Kikkawa, Physics Today 33-38 June (1999)
12. M. Osofsky, J. of Supercon.: Incorporating Novel Magnetism **13** 209-219 (2000)
13. C. Gould, G. Schmidt, G. Richter, R. Fiederling, P. Grabs, L. W. Molenkamp, Appl. Surf. Sci. **7640** 1-8 (2000)
14. S. von Molnar, D. Read, J. Mag. And Mag. Mat. **242-245** 13-20 (2002)
15. B. T. Jonker, X. Liu, W. C. Chou, A. Petrou, J. Warnock, J. J. Krebs, G. A. Prinz, J. Appl. Phys. **69** 6097-6102 (1991)
16. G. Schmidt, L. W. Molenkamp, Physica E **10** 484-488 (2001)
17. H. Ohno, F. Matsukura, Y. Ohno, Sol. St. Comm. **119** 281-289 (2001)
18. G. Schmidt, L. W. Molenkamp, J. Appl. Phys. **89** 7443-7447 (2001)

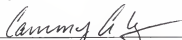
19. T. Dietl, H. Ohno, *Physica E* **9** 185-193 (2001)
20. H. Munekata, S. von Molnar, A. Segmuller, L. L. Chang, L. Esaki, *Phys. Rev. Lett.* **63** 1849-1852 (1989)
21. H. Ohno, H. Munekata, S. von Molnar, L. L. Chang, *J. Appl. Phys.* **69** 6103-6108 (1991)
22. H. Ohno, H. Munekata, T. Penney, S. von Molnar, L. L. Chang, *Phys. Rev. Lett.* **68** 2664-2667 (1992)
23. H. Munekata, T. Abe, S. Koshihara, A. Oiwa, M. Hirasawa, S. Katsumoto, Y. Iye, C. Urano, H. Takagi, *J. Appl. Phys.* **81** 4862-4864 (1997)
24. H. Ohno, A. Shen, F. Matsukura, A. Oiwa, A. Endo, S. Katsumoto, Y. Iye, *Appl. Phys. Lett.* **69** 363-365 (1996)
25. T. Hayashi, M. Tanaka, K. Seto, T. Nishinaga, H. Shimada, H. Hayashi, K. Niihara, *Physica E* **2** 404-407 (1998)
26. A. Van Esch, L. Van Bockstal, J. De Boeck, G. Verbanck, A. S. van Steenberghe, P. J. Wellmann, B. Grietens, R. Bogaerts, F. Herlach, G. Borghs, *Phys. Rev. B* **56** 13103-13112 (1997)
27. F. Matsukura, *Phys. Rev. B* **57** R2037 (1998)
28. H. Saito, W. Zaets, R. Akimoto, K. Ando, Y. Mishima, M. Tanaka, *J. Appl. Phys.* **89** 7392-7394 (2001)
29. T. Dietl, H. Ohno, F. Matsukura, J. Cibert, D. Ferrand, *Science* **287** 1019-1022 (2000)
30. C. Liu, E. Alves, A. R. Ramos, M. F. da Silva, J. C. Soares, T. Matsutani, M. Kiuchi, *Nuc. Inst. Meth. Phys. Res. B* **191** 544-548 (2002)
31. E. Kulatov, H. Nakayama, H. Mariette, H. Ohta, Y. A. Uspenskii, *Phys. Rev. B* **66** 1-9 (2002)
32. M. E. Overberg, C. R. Abernathy, S. J. Pearton, N. A. Theodoropoulou, K. T. McCarthy, A. F. Hebard, *Appl. Phys. Lett.* **79** 1312-1314 (2001)
33. H. Hori, S. Sonoda, T. Sasaki, Y. Yamamoto, S. Shimizu, K. Suga, K. Kindo, *Physica B* **324** 142-150 (2002)
34. S. Sonoda, S. Shimizu, T. Sasaki, Y. Yamamoto, H. Hori, *J. Cryst. Gr.* **237-239** 1358-1362 (2002)

35. G. T. Thaler, M. E. Overberg, B. Gila, R. Frazier, C. R. Abernathy, S. J. Pearton, J. S. Lee, S. Y. Lee, Y. D. Park, Z. G. Khim, J. Kim, F. Ren, *Appl. Phys. Lett.* **80** 3964-3966 (2002)
36. M. Hashimoto, Y-K. Zhou, M. Kanamura, H. Asahi, *Sol. St. Comm.* **122** 37-39 (2002)
37. G. T. Thaler, R. M. Frazier, C. R. Abernathy, S. J. Pearton, *Appl. Phys. Lett.* **86** 131901 (2005)
38. H. X. Liu et al *Appl. Phys. Lett.* **85** 4076-4078 (2004)
39. S. Dhar, O. Brandt, M. Ramsteiner, V. F. Sapega, K. H. Ploog, *Phys. Rev. Lett.* **94** 037205-1-4 (2005)
40. to be published
41. J. E. Medvedeva, A. J. Freeman, X. Y. Ciu, C. Stampfl, N. Newman, *Phys. Rev. Lett.* **94** 146602-1-4 (2005)
42. Z. Liu, J. De Boeck, V. V. Moshchalkov, G. Borghs, *J. Mag. Mag. Mat.* **242-245** 967-969 (2002)
43. V. I. Litvinov, V. K. Dugaev, *Phys. Rev. Lett.* **86** 5593-5596 (2001)
44. S. G. Yang, A. B. Pakhomov, S. T. Hung, C. Y. Wong, *Appl. Phys. Lett.* **81** 2418-2420 (2002)
45. S. Y. Wu, H. X. Liu, L. Gu, R. K. Singh, L. Budd, M. van Schilfgaarde, M. R. McCartney, D. J. Smith, N. Newman, *Appl. Phys. Lett.* **82** 3047-3049 (2003)
46. C. Zener, *Phys. Rev.* **81** 440-444 (1951)
47. C. Zener, *Phys. Rev.* **83** 299-301 (1951)
48. T. Dietl, *J. Appl. Phys.* **89** 7437-7442 (2001)
49. H. Ohno, *Science* **281** 951-956 (1998)
50. M. Berciu, R. N. Bhatt, *Phys. Rev. B* **87** 107203-1-4 (2001)
51. A. Kaminski, S. Das Sarma, *Phys. Rev. Lett.* **88** 247202-1-4 (2002)
52. A. L. Chudnovskiy, D. Pfannkuche, *Phys. Rev. B* **65** 165216-1-7 (2002)

## BIOGRAPHICAL SKETCH

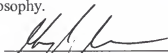
I was born March 30, 1978, in Jacksonville, Florida. I attended Wolfson High School from 1992 and graduated in 1996. I began studying anthropology at the University of Florida in the summer of 1996 and by the end of the spring semester in 1997 I changed my major to physics. In 2001, I graduated from the University of Florida with a Bachelor of Science in the field of physics. In the summer of 2001 I started my graduate career working in Cammy Abernathy's molecular beam epitaxy lab. I received a Master of Science degree in the fall of 2003 and continued doctoral research. During the fall semester of 2004, I interned at Sandia National Laboratory under the guidance of Albert Baca. After returning to the University of Florida, I began writing my dissertation and completing all research projects.

I certify that I have read this study and that in my opinion it conforms to acceptable standards of scholarly presentation and is fully adequate, in scope and quality, as a dissertation for the degree of Doctor of Philosophy.



Cammy Abernathy, Chairman  
Professor of Materials Science and  
Engineering

I certify that I have read this study and that in my opinion it conforms to acceptable standards of scholarly presentation and is fully adequate, in scope and quality, as a dissertation for the degree of Doctor of Philosophy.



Steve Pearson  
Distinguished Professor of Materials  
Science and Engineering

I certify that I have read this study and that in my opinion it conforms to acceptable standards of scholarly presentation and is fully adequate, in scope and quality, as a dissertation for the degree of Doctor of Philosophy.



David Norton  
Professor of Materials Science and  
Engineering

I certify that I have read this study and that in my opinion it conforms to acceptable standards of scholarly presentation and is fully adequate, in scope and quality, as a dissertation for the degree of Doctor of Philosophy.



Fan Ren  
Professor of Chemical Engineering

I certify that I have read this study and that in my opinion it conforms to acceptable standards of scholarly presentation and is fully adequate, in scope and quality, as a dissertation for the degree of Doctor of Philosophy.



Art Hebard  
Professor of Physics

This thesis was submitted to the Graduate Faculty of the College of Engineering and to the Graduate School and was accepted as partial fulfillment of the requirements for the degree of Doctor of Philosophy.

August 2005

A handwritten signature in dark ink, appearing to read "Pramod P. Khargonekar", written over a horizontal line.

Pramod P. Khargonekar  
Dean, College of Engineering

---

Winfred M. Phillips  
Dean, Graduate School